EUROPEAN ORGANIZATION FOR NUCLEAR RESEARCH

CERN–EP/2001–060
July 25, 2001

$\mathcal{T}$-violation and $\mathcal{CPT}$-invariance measurements in the CPLEAR experiment: a detailed description of the analysis of neutral-kaon decays to $\mathrm{e}\pi\nu$.

CPLEAR Collaboration

A. Angelopoulos[1)], E. Aslanides[11)], G. Backenstoss[2)], P. Bargassa[13)], O. Behnke[17)], A. Benelli[2)], V. Bertin[11)], F. Blanc[7,13)], P. Bloch[4)], P. Carlson[15)], M. Carroll[9)], E. Cawley[9)], M.B. Chertok[3)], M. Danielsson[15)], M. Dejardin[14)], J. Derre[14)], A. Ealet[11)], C. Eleftheriadis[16)], W. Fetscher[17)], M. Fidecaro[4)], A. Filipčič[10)], D. Francis[3)], J. Fry[9)], E. Gabathuler[9)], R. Gamet[9)], H.-J. Gerber[17)], A. Go[4)], A. Haselden[9)], P.J. Hayman[9)], F. Henry-Couannier[11)], R.W. Hollander[6)], K. Jon-And[15)], P.-R. Kettle[13)], P. Kokkas[8)], R. Kreuger[6)], R. Le Gac[11)], F. Leimgruber[2)], I. Mandić[10)], N. Manthos[8)], G. Marel[14)], M. Mikuž[10)], J. Miller[3)], F. Montanet[11)], A. Muller[14)] T. Nakada[13)], B. Pagels[17)], I. Papadopoulos[16)], P. Pavlopoulos[2)], G. Polivka[2)], R. Rickenbach[2)], B.L. Roberts[3)], T. Ruf[4)], L. Sakeliou[1)], M. Schäfer[17)], L.A. Schaller[7)], T. Schietinger[2)], A. Schopper[4)], L. Tauscher[2)], C. Thibault[12)], F. Touchard[11)], C. Touramanis[9)], C.W.E. Van Eijk[6)], S. Vlachos[2)], P. Weber[17)], O. Wigger[13)], M. Wolter[17)], D. Zavrtanik[10)], D. Zimmerman[3)]

Abstract

A detailed description of the analysis of neutral kaons decaying to $\mathrm{e}\pi\nu$ is given, based on the complete set of data collected with the CPLEAR experiment. Using a novel approach involving initially strangeness-tagged K^0 and $\overline{\mathrm{K}}^0$, time-dependent decay-rate asymmetries were measured. These asymmetries enabled $\mathcal{T}$- and $\mathcal{CPT}$-violation parameters to be measured in the context of a systematic study. The highlights of this study are the first direct observation of $\mathcal{T}$ violation and the direct determination of the $\mathcal{CPT}$ parameter $\mathrm{Re}(\delta)$ with an accuracy improved by two orders of magnitude with respect to the current value.

(Submitted to Eur. Phys. J. C)

[1)] University of Athens, Greece
[2)] University of Basle, Switzerland
[3)] Boston University, USA
[4)] CERN, Geneva, Switzerland
[5)] LIP and University of Coimbra, Portugal
[6)] Delft University of Technology, Netherlands
[7)] University of Fribourg, Switzerland
[8)] University of Ioannina, Greece
[9)] University of Liverpool, UK
[10)] J. Stefan Inst. and Phys. Dep., University of Ljubljana, Slovenia
[11)] CPPM, IN2P3-CNRS et Université d'Aix-Marseille II, France
[12)] CSNSM, IN2P3-CNRS, Orsay, France
[13)] Paul Scherrer Institut (PSI), Switzerland
[14)] CEA, DSM/DAPNIA, CE-Saclay, France
[15)] Royal Institute of Technology, Stockholm, Sweden
[16)] University of Thessaloniki, Greece
[17)] ETH-IPP Zürich, Switzerland

1 Introduction

The CPLEAR experiment, at the Low Energy Antiproton Ring (LEAR) at CERN, has developed a novel approach to the study of $\mathcal{CP}$, $\mathcal{T}$ and $\mathcal{CPT}$ symmetries in the decays of neutral kaons. In this approach, the strangeness of the neutral kaons at production is tagged and then decay-rate asymmetries are measured for decays to a variety of final states. From these asymmetries, parameters describing violations of $\mathcal{CP}$, $\mathcal{T}$ and $\mathcal{CPT}$ are determined with small systematic uncertainties [1].

In this paper we give a detailed description of the analysis of neutral kaons decaying to $\mathrm{e}\pi\nu$, based on the complete set of data collected by CPLEAR between 1991 and 1996. Letters giving these results for Δm, A_{T} and $\mathrm{Re}(\delta)$ have already been published [2–4]. Of these quantities, A_{T}, the asymmetry of $\mathcal{T}$-conjugated decay rates, was measured for the first time. The accuracy of the $\mathcal{CPT}$-parameter $\mathrm{Re}(\delta)$ was improved by two orders of magnitude with respect to the previous measurement [5]. The measurement of the $\mathrm{K_L}$ and $\mathrm{K_S}$ mass difference, Δm, reached a precision comparable to compilations [6, 7] of previous experiments [8–14] (the compilation fits included other experimental information on parameters of the neutral-kaon system, such as ϕ_{+-}, $\mathrm{K_S}$ and $\mathrm{K_L}$ mean lifetimes and branching ratios).

All these measurements, in combination with the values of other parameters measured by CPLEAR, provide a stringent indirect test of $\mathcal{CPT}$ invariance [15, 16]. Moreover, the CPLEAR $\mathrm{e}\pi\nu$ data, in conjunction with CPLEAR $\pi^+\pi^-$ data and results from other experiments at late decay times, may be used to set limits on parameters describing the possible evolution of pure states into mixed states, sensitive to physics at ultra-high energies [17–19]. Such limits were calculated in Ref. [17] using a subset of the total CPLEAR data [13, 14] and data from Refs. [7, 20].

In Section 2, the phenomenology of neutral-kaon decays to $\mathrm{e}\pi\nu$ is described. In Section 3 we describe the method used to construct the experimental asymmetries to be compared with the phenomenological expressions. The CPLEAR experiment is presented in Section 4 followed by the event selection and comparison with simulated data in Section 5. Corrections applied to the data are detailed in Section 6 and the final results are reported in Section 7. A summary of the results and their significance is given in Section 8.

2 Phenomenology of neutral-kaon decays to $\mathrm{e}\pi\nu$

The strong and electromagnetic interactions conserve strangeness and their Hamiltonians have well-defined strangeness eigenstates $\mathrm{K^0}$ and $\overline{\mathrm{K}}^0$. The weak interaction does not conserve strangeness and causes the two strangeness eigenstates to mix ($|\Delta S| = 2$ processes), and also to decay to non-strange final states ($|\Delta S| = 1$ processes). The time evolution of the $\mathrm{K^0}$–$\overline{\mathrm{K}}^0$ state, including its decay products, is described by the Schrödinger equation with a total Hamiltonian $\mathcal{H}_{\mathrm{st}} + \mathcal{H}_{\mathrm{em}} + \mathcal{H}_{\mathrm{wk}}$. The weak interaction ($\mathcal{H}_{\mathrm{wk}}$) is much weaker than either the strong ($\mathcal{H}_{\mathrm{st}}$) or electromagnetic ($\mathcal{H}_{\mathrm{em}}$) interaction. Therefore a perturbation calculation may be used to eliminate the explicit appearance of the decay products in the time dependence of the neutral-kaon system, which leads to

$$|\psi(t)\rangle = a(t)\left|\mathrm{K^0}\right\rangle + b(t)\left|\overline{\mathrm{K}}^0\right\rangle,$$

satisfying

$$\mathrm{i}\frac{\partial}{\partial t}\begin{pmatrix} a(t) \\ b(t) \end{pmatrix} = \Lambda \begin{pmatrix} a(t) \\ b(t) \end{pmatrix}, \tag{1}$$

where Λ is a complex, two-by-two matrix and is expressed in terms of two hermitian matrices M (the mass matrix) and Γ (the decay matrix) as $\Lambda = \mathrm{M} - \frac{\mathrm{i}}{2}\Gamma$. The diagonal elements of these matrices, $\mathrm{M_{K^0K^0}}$ and $\mathrm{M_{\overline{K}^0\overline{K}^0}}$, $\Gamma_{\mathrm{K^0K^0}}$ and $\Gamma_{\mathrm{\overline{K}^0\overline{K}^0}}$, signify the masses and decay widths of $\mathrm{K^0}$ and $\overline{\mathrm{K}}^0$. The eigenvalues of Eq. (1) are

$$\lambda_{\mathrm{L,S}} = m_{\mathrm{L,S}} - \tfrac{\mathrm{i}}{2}\Gamma_{\mathrm{L,S}}$$

and the corresponding eigenstates are $|\mathrm{K_S}\rangle$ and $|\mathrm{K_L}\rangle$, which have definite masses $m_{\mathrm{L,S}}$ and decay widths $\Gamma_{\mathrm{L,S}}$. Assuming any violation of $\mathcal{T}$ or $\mathcal{CPT}$ invariance to be small, the eigenstates are given by

$$|\mathrm{K_S}\rangle = \frac{1}{\sqrt{2}}\left[(1+\varepsilon+\delta)\left|\mathrm{K^0}\right\rangle + (1-\varepsilon-\delta)\left|\overline{\mathrm{K}}^0\right\rangle\right], \tag{2a}$$

$$|\mathrm{K_L}\rangle = \frac{1}{\sqrt{2}}\left[(1+\varepsilon-\delta)\left|\mathrm{K^0}\right\rangle - (1-\varepsilon+\delta)\left|\overline{\mathrm{K}}^0\right\rangle\right], \tag{2b}$$

where the parameters ε and δ describe $\mathcal{T}$ and $\mathcal{CP}$ violation with $\mathcal{CPT}$ invariance, and $\mathcal{CPT}$ and $\mathcal{CP}$ violation with $\mathcal{T}$ invariance, respectively. These parameters are given by

$$\varepsilon = \frac{\Lambda_{\overline{\mathrm{K}}^0\mathrm{K}^0} - \Lambda_{\mathrm{K}^0\overline{\mathrm{K}}^0}}{2\Delta\lambda} \quad \text{and} \quad \delta = \frac{\Lambda_{\overline{\mathrm{K}}^0\overline{\mathrm{K}}^0} - \Lambda_{\mathrm{K}^0\mathrm{K}^0}}{2\Delta\lambda} \,,$$

with $\Delta\lambda = \lambda_\mathrm{L} - \lambda_\mathrm{S} = \Delta m + \frac{\mathrm{i}}{2}\Delta\Gamma$, $\Delta m = m_\mathrm{L} - m_\mathrm{S}$, $\Delta\Gamma = \Gamma_\mathrm{S} - \Gamma_\mathrm{L}$. The off-diagonal elements of Λ, $|\mathrm{M}_{\mathrm{K}^0\overline{\mathrm{K}}^0}|\mathrm{e}^{\mathrm{i}\phi_\mathrm{M}} - \frac{\mathrm{i}}{2}|\Gamma_{\mathrm{K}^0\overline{\mathrm{K}}^0}|\mathrm{e}^{\mathrm{i}\phi_\Gamma}$ and $|\mathrm{M}_{\mathrm{K}^0\overline{\mathrm{K}}^0}|\mathrm{e}^{-\mathrm{i}\phi_\mathrm{M}} - \frac{\mathrm{i}}{2}|\Gamma_{\mathrm{K}^0\overline{\mathrm{K}}^0}|\mathrm{e}^{-\mathrm{i}\phi_\Gamma}$, are related to Δm and $\Delta\Gamma$ as $2|\mathrm{M}_{\mathrm{K}^0\overline{\mathrm{K}}^0}| = \Delta m$ and $2|\Gamma_{\mathrm{K}^0\overline{\mathrm{K}}^0}| = \Delta\Gamma$. The arbitrariness of the phases of the K^0 and $\overline{\mathrm{K}}^0$ states allows us to choose $\phi_\Gamma = 0$ or close to 0.

For initially pure K^0 and $\overline{\mathrm{K}}^0$ states, the solutions of Eq. (1) are

$$\begin{aligned}
\left|\mathrm{K}^0(t)\right\rangle &= [f_+(t) + 2\delta f_-(t)]\left|\mathrm{K}^0\right\rangle + (1-2\varepsilon) f_-(t)\left|\overline{\mathrm{K}}^0\right\rangle \\
&= \frac{1}{\sqrt{2}}[(1-\varepsilon+\delta)\mathrm{e}^{-\mathrm{i}\lambda_\mathrm{S} t}\left|\mathrm{K_S}\right\rangle + (1-\varepsilon-\delta)\mathrm{e}^{-\mathrm{i}\lambda_\mathrm{L} t}\left|\mathrm{K_L}\right\rangle] \,, \qquad (3a) \\
\left|\overline{\mathrm{K}}^0(t)\right\rangle &= [f_+(t) - 2\delta f_-(t)]\left|\overline{\mathrm{K}}^0\right\rangle + (1+2\varepsilon) f_-(t)\left|\mathrm{K}^0\right\rangle \\
&= \frac{1}{\sqrt{2}}[(1+\varepsilon-\delta)\mathrm{e}^{-\mathrm{i}\lambda_\mathrm{S} t}\left|\mathrm{K_S}\right\rangle - (1+\varepsilon+\delta)\mathrm{e}^{-\mathrm{i}\lambda_\mathrm{L} t}\left|\mathrm{K_L}\right\rangle] \,, \qquad (3b)
\end{aligned}$$

with the time-dependent functions given by $f_\pm(t) = \frac{1}{2}(\mathrm{e}^{-\mathrm{i}\lambda_\mathrm{S} t} \pm \mathrm{e}^{-\mathrm{i}\lambda_\mathrm{L} t})$. For the decay of a K^0 or a $\overline{\mathrm{K}}^0$ to a final state $\mathrm{e}\pi\nu$, we can define four amplitudes,

$$\begin{aligned}
\mathcal{A}_+ &= \left\langle \mathrm{e}^+\pi^-\nu\right| \mathcal{H}_\mathrm{wk}\left|\mathrm{K}^0\right\rangle \,, \qquad & \overline{\mathcal{A}}_- &= \left\langle \mathrm{e}^-\pi^+\overline{\nu}\right| \mathcal{H}_\mathrm{wk}\left|\overline{\mathrm{K}}^0\right\rangle \,, \qquad (4a) \\
\mathcal{A}_- &= \left\langle \mathrm{e}^-\pi^+\overline{\nu}\right| \mathcal{H}_\mathrm{wk}\left|\mathrm{K}^0\right\rangle \,, \qquad & \overline{\mathcal{A}}_+ &= \left\langle \mathrm{e}^+\pi^-\nu\right| \mathcal{H}_\mathrm{wk}\left|\overline{\mathrm{K}}^0\right\rangle \,, \qquad (4b)
\end{aligned}$$

each one being a function of the kinematic configuration (including spin) of the final state. Of these amplitudes, $\mathcal{A}_+$ and $\overline{\mathcal{A}}_-$ respect the $\Delta S = \Delta Q$ rule, $\mathcal{A}_-$ and $\overline{\mathcal{A}}_+$ violate it. Each amplitude can be further decomposed in two terms, of which one is $\mathcal{CPT}$ invariant and the other is $\mathcal{CPT}$ non-invariant [21, 22].

$$\begin{aligned}
\mathcal{A}_+ &= a + b \,, \qquad & \overline{\mathcal{A}}_- &= a^* - b^* \,, \qquad (5a) \\
\mathcal{A}_- &= c + d \,, \qquad & \overline{\mathcal{A}}_+ &= c^* - d^* \,. \qquad (5b)
\end{aligned}$$

The $\mathcal{CPT}$-invariant and -violating terms are given by a and b if the $\Delta S = \Delta Q$ rule holds, and by c and d if it is violated. As for $\mathcal{T}$, the imaginary parts of all amplitudes are $\mathcal{T}$ violating. It is also convenient to introduce the quantities

$$x = \frac{\overline{\mathcal{A}}_+}{\mathcal{A}_+} \,, \qquad \overline{x} = \left(\frac{\mathcal{A}_-}{\overline{\mathcal{A}}_-}\right)^* \,, \qquad y = \frac{\overline{\mathcal{A}}_-^* - \mathcal{A}_+}{\overline{\mathcal{A}}_-^* + \mathcal{A}_+} \,, \qquad (6)$$

where x and $\overline{x}$ parametrize the violation of the $\Delta S = \Delta Q$ rule in decays to positive and negative leptons, respectively, and $y = -b/a$ parametrizes $\mathcal{CPT}$ violation when the $\Delta S = \Delta Q$ rule holds. $\mathrm{Re}(a)$ is $\mathcal{T}$, $\mathcal{CPT}$ and $\mathcal{CP}$ invariant and dominates all other terms, hence x, $\overline{x}$ and y are all $\ll 1$. The parameters $x_+ = (x + \overline{x})/2$ and $x_- = (x - \overline{x})/2$ describe the violation of the $\Delta S = \Delta Q$ rule in $\mathcal{CPT}$-conserving and $\mathcal{CPT}$-violating amplitudes, respectively.

Finally, neutral-kaon decays to $\mathrm{e}\pi\nu$ are described by four independent decay rates, depending on the strangeness of the kaon (K^0 or $\overline{\mathrm{K}}^0$) at the production time, $t = 0$, and on the charge of the decay lepton (e^+ or e^-):

$$\begin{aligned}
R_+(\tau) &\equiv R\left[{\mathrm{K}^0}_{t=0} \to (\mathrm{e}^+\pi^-\nu)_{t=\tau}\right] \,, \qquad & \overline{R}_-(\tau) &\equiv R\left[\overline{\mathrm{K}}^0_{t=0} \to (\mathrm{e}^-\pi^+\overline{\nu})_{t=\tau}\right] \,, \qquad (7a) \\
R_-(\tau) &\equiv R\left[{\mathrm{K}^0}_{t=0} \to (\mathrm{e}^-\pi^+\overline{\nu})_{t=\tau}\right] \,, \qquad & \overline{R}_+(\tau) &\equiv R\left[\overline{\mathrm{K}}^0_{t=0} \to (\mathrm{e}^+\pi^-\nu)_{t=\tau}\right] \,, \qquad (7b)
\end{aligned}$$

where τ is the decay eigentime of the neutral kaon. The dependence of the rates on τ and on various parameters is obtained by making use of Eqs. (3, 4) and integrating over the final-state phase space Ω:

$$R_+(\tau) = \int_\Omega |[f_+(\tau) + 2\delta f_-(\tau)]\mathcal{A}_+ + (1-2\epsilon) f_-(\tau)\overline{\mathcal{A}}_+|^2 \mathrm{d}\Omega\,, \tag{8a}$$

$$\overline{R}_-(\tau) = \int_\Omega |[f_+(\tau) - 2\delta f_-(\tau)]\overline{\mathcal{A}}_- + (1+2\epsilon) f_-(\tau)\mathcal{A}_-|^2 \mathrm{d}\Omega\,, \tag{8b}$$

$$R_-(\tau) = \int_\Omega |[f_+(\tau) + 2\delta f_-(\tau)]\mathcal{A}_- + (1-2\epsilon) f_-(\tau)\overline{\mathcal{A}}_-|^2 \mathrm{d}\Omega\,, \tag{8c}$$

$$\overline{R}_+(\tau) = \int_\Omega |[f_+(\tau) - 2\delta f_-(\tau)]\overline{\mathcal{A}}_+ + (1+2\epsilon) f_-(\tau)\mathcal{A}_+|^2 \mathrm{d}\Omega\,. \tag{8d}$$

Owing to the rate integration over the phase-space configurations of the final state, it is convenient to redefine the parameters x, $\bar{x}$ and y through the following equations:

$$\mathcal{F}_+ = \int_\Omega |\mathcal{A}_+|^2 \mathrm{d}\Omega\,, \qquad \mathcal{F}_- = \int_\Omega |\overline{\mathcal{A}}_-|^2 \mathrm{d}\Omega\,, \qquad \mathcal{F} = \int_\Omega |\overline{\mathcal{A}}_-^* + \mathcal{A}_+|^2 \mathrm{d}\Omega\,,$$
$$x = \frac{\int_\Omega \mathcal{A}_+^* \overline{\mathcal{A}}_+ \mathrm{d}\Omega}{\mathcal{F}_+}\,, \qquad \bar{x} = \frac{\int_\Omega \overline{\mathcal{A}}_-^* \mathcal{A}_- \mathrm{d}\Omega}{\mathcal{F}_-}\,, \qquad \mathrm{Re}(y) = -\frac{1}{2} \times \frac{\mathcal{F}_+ - \mathcal{F}_-}{\mathcal{F}_+ + \mathcal{F}_-}\,.$$

If the decay amplitudes of Eqs. (4, 5) are constant over the phase space, these definitions are essentially the same as Eq. (6) – more common in the current literature. The same conclusion is reached if the kinematic dependence can be factorized as a factor common to all four amplitudes (as is usual in $\mathrm{K}^0_{\mathrm{e}3}$ form-factor studies [23]).

Keeping only first-order terms in all parameters, the four independent decay rates can now be written as

$$\begin{aligned} R_+(\tau) = \frac{\mathcal{F}}{4}\Big(& [1 + 2\mathrm{Re}(x) + 4\mathrm{Re}(\delta) - 2\mathrm{Re}(y)]\,\mathrm{e}^{-\Gamma_\mathrm{S}\tau} + [1 - 2\mathrm{Re}(x) - 4\mathrm{Re}(\delta) - 2\mathrm{Re}(y)]\,\mathrm{e}^{-\Gamma_\mathrm{L}\tau} \\ & + \{2[1 - 2\mathrm{Re}(y)]\cos(\Delta m\tau) - [8\mathrm{Im}(\delta) + 4\mathrm{Im}(x)]\sin(\Delta m\tau)\}\,\mathrm{e}^{-\frac{1}{2}(\Gamma_\mathrm{S}+\Gamma_\mathrm{L})\tau}\Big), \end{aligned} \tag{9a}$$

$$\begin{aligned} \overline{R}_-(\tau) = \frac{\mathcal{F}}{4}\Big(& [1 + 2\mathrm{Re}(\overline{x}) - 4\mathrm{Re}(\delta) + 2\mathrm{Re}(y)]\,\mathrm{e}^{-\Gamma_\mathrm{S}\tau} + [1 - 2\mathrm{Re}(\overline{x}) + 4\mathrm{Re}(\delta) + 2\mathrm{Re}(y)]\,\mathrm{e}^{-\Gamma_\mathrm{L}\tau} \\ & + \{2[1 + 2\mathrm{Re}(y)]\cos(\Delta m\tau) + [8\mathrm{Im}(\delta) + 4\mathrm{Im}(\overline{x})]\sin(\Delta m\tau)\}\,\mathrm{e}^{-\frac{1}{2}(\Gamma_\mathrm{S}+\Gamma_\mathrm{L})\tau}\Big), \end{aligned} \tag{9b}$$

$$\begin{aligned} R_-(\tau) = \frac{\mathcal{F}}{4}\Big(& [1 + 2\mathrm{Re}(\overline{x}) - 4\mathrm{Re}(\varepsilon) + 2\mathrm{Re}(y)]\,\mathrm{e}^{-\Gamma_\mathrm{S}\tau} + [1 - 2\mathrm{Re}(\overline{x}) - 4\mathrm{Re}(\varepsilon) + 2\mathrm{Re}(y)]\,\mathrm{e}^{-\Gamma_\mathrm{L}\tau} \\ & - \{2[1 - 4\mathrm{Re}(\varepsilon) + 2\mathrm{Re}(y)]\cos(\Delta m\tau) + 4\mathrm{Im}(\overline{x})\sin(\Delta m\tau)\}\,\mathrm{e}^{-\frac{1}{2}(\Gamma_\mathrm{S}+\Gamma_\mathrm{L})\tau}\Big), \end{aligned} \tag{9c}$$

$$\begin{aligned} \overline{R}_+(\tau) = \frac{\mathcal{F}}{4}\Big(& [1 + 2\mathrm{Re}(x) + 4\mathrm{Re}(\varepsilon) - 2\mathrm{Re}(y)]\,\mathrm{e}^{-\Gamma_\mathrm{S}\tau} + [1 - 2\mathrm{Re}(x) + 4\mathrm{Re}(\varepsilon) - 2\mathrm{Re}(y)]\,\mathrm{e}^{-\Gamma_\mathrm{L}\tau} \\ & - \{2[1 + 4\mathrm{Re}(\varepsilon) - 2\mathrm{Re}(y)]\cos(\Delta m\tau) - 4\mathrm{Im}(x)\sin(\Delta m\tau)\}\,\mathrm{e}^{-\frac{1}{2}(\Gamma_\mathrm{S}+\Gamma_\mathrm{L})\tau}\Big). \end{aligned} \tag{9d}$$

The phenomenological description of neutral-kaon decays to $\mu\pi\nu$ is the same as that of decays to $\mathrm{e}\pi\nu$, once the different kinematic conditions are taken into account. The symmetry properties of the parameters entering Eqs. (9a–9d) are summarized in Table 1.

Alternatively we can express the rates in terms of $\mathrm{K_S}$ and $\mathrm{K_L}$ amplitudes to a final state f:

$$\mathcal{A}_{f\mathrm{S}} = \langle f|\mathcal{H}_{\mathrm{wk}}|\mathrm{K_S}\rangle\,, \quad \mathcal{A}_{f\mathrm{L}} = \langle f|\mathcal{H}_{\mathrm{wk}}|\mathrm{K_L}\rangle\,. \tag{10}$$

Then for the decay rates, at a time $t = \tau$, of an initially pure K^0 or $\overline{\mathrm{K}}^0$ state,

$$R_f(\tau) \equiv R\left[\mathrm{K}^0{}_{t=0} \to f_{t=\tau}\right]\,, \qquad \overline{R}_f(\tau) \equiv R\left[\overline{\mathrm{K}}^0_{t=0} \to f_{t=\tau}\right]\,, \tag{11}$$

Table 1: Symmetry properties of phenomenological parameters [22].

$\Delta S = \Delta Q$	$x = \overline{x} = 0$
$\mathcal{CPT}$ exact in $\Delta S = 1$	$x = \overline{x},\ y = 0$
$\mathcal{T}$ exact in $\Delta S = 1$	x, $\overline{x}$, y real
$\mathcal{CP}$ exact in $\Delta S = 1$	$x = \overline{x}^*$, y imaginary
$\mathcal{CPT}$ exact in $\Delta S = 2$	$\delta = 0$
$\mathcal{T}$ exact in $\Delta S = 2$	$\varepsilon = 0$
$\mathcal{CP}$ exact in $\Delta S = 2$	$\varepsilon = \delta = 0$

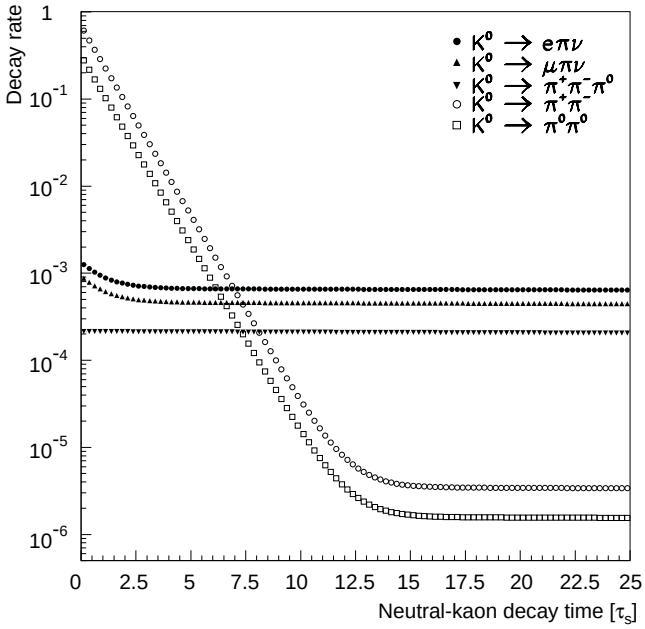

Figure 1: Neutral-kaon decay rates for the main decay modes as a function of the decay time τ (in units of the $\mathrm{K_S}$ mean lifetime τ_S). The branching ratios are from Ref. [7]. The rates are averaged over an equal number of initial K^0 and $\overline{\mathrm{K}}^0$; their sum is normalized at $t = 0$ to unity.

we obtain from Eqs. (3a, 3b)

$$\begin{aligned}\frac{R_f(\tau)}{\overline{R}_f(\tau)} \;=\; & \frac{[1 \mp 2\mathrm{Re}(\varepsilon)]}{2} \times \Big\{ \big[1 \pm 2\mathrm{Re}(\delta)\big]\,|\mathcal{A}_{f\mathrm{S}}|^2 \mathrm{e}^{-\Gamma_\mathrm{S}\tau} + \big[1 \mp 2\mathrm{Re}(\delta)\big]\,|\mathcal{A}_{f\mathrm{L}}|^2 \mathrm{e}^{-\Gamma_\mathrm{L}\tau} \\ & \pm \mathrm{e}^{-\frac{1}{2}(\Gamma_\mathrm{S}+\Gamma_\mathrm{L})\tau} \Big(\big[1 \pm 2\mathrm{iIm}(\delta)\big]\,\mathcal{A}^*_{f\mathrm{L}}\mathcal{A}_{f\mathrm{S}} \mathrm{e}^{\mathrm{i}\Delta m\tau} + \big[1 \mp 2\mathrm{iIm}(\delta)\big]\,\mathcal{A}^*_{f\mathrm{S}}\mathcal{A}_{f\mathrm{L}} \mathrm{e}^{-\mathrm{i}\Delta m\tau} \Big) \Big\}\,.\end{aligned}$$

This expression is commonly used when f is a $\mathcal{CP}$ eigenstate, for instance in the decay to $\pi^+\pi^-$ ($f \equiv \pi^+\pi^-$), also to be considered in the present study (Section 6). In this case we define the $\mathcal{CP}$-violating parameter:

$$\eta_{+-} \;=\; |\eta_{+-}|\mathrm{e}^{\mathrm{i}\phi_{+-}} \;=\; \frac{\mathcal{A}_{f\mathrm{L}}}{\mathcal{A}_{f\mathrm{S}}} \;=\; \frac{\langle \pi^+\pi^- |\, \mathcal{H}_\mathrm{wk}\, | \mathrm{K_L} \rangle}{\langle \pi^+\pi^- |\, \mathcal{H}_\mathrm{wk}\, | \mathrm{K_S} \rangle}, \tag{12}$$

where $|\eta_{+-}| \ll 1$ and $\Gamma_\mathrm{S}^{2\pi} = |\mathcal{A}_{f\mathrm{S}}|^2$ is the $\mathrm{K_S} \to \pi^+\pi^-$ partial width. The corresponding rates become

$$\frac{R_f(\tau)}{\overline{R}_f(\tau)} \;=\; \frac{[1 \mp 2\mathrm{Re}(\varepsilon - \delta)]}{2} \Gamma_\mathrm{S}^{2\pi} \times \big[\mathrm{e}^{-\Gamma_\mathrm{S}\tau} + |\eta_{+-}|^2 \mathrm{e}^{-\Gamma_\mathrm{L}\tau} \pm\, 2|\eta_{+-}| \mathrm{e}^{-\frac{1}{2}(\Gamma_\mathrm{S}+\Gamma_\mathrm{L})\tau} \cos(\Delta m\tau - \phi_{+-}) \big]\,. \tag{13}$$

The rates averaged over an equal number of initial K^0 and $\overline{\mathrm{K}}^0$ are shown in Fig. 1 for the main decay

modes. The measurement of the rates (9a–9d) as a function of τ allows $\mathcal{T}$ and $\mathcal{CPT}$ parameters and Δm to be determined. This is best achieved by forming rate asymmetries (thus allowing some systematic errors to be reduced), for instance

$$\begin{aligned}\frac{\overline{R}_+(\tau) - R_-(\tau)}{\overline{R}_+(\tau) + R_-(\tau)} &= 4\mathrm{Re}(\varepsilon) - 2(\mathrm{Re}(y) + \mathrm{Re}(x_-)) \\ &+ 2\frac{\mathrm{Re}(x_-)(\mathrm{e}^{-\frac{1}{2}\Delta\Gamma\tau} - \cos(\Delta m\tau)) + \mathrm{Im}(x_+)\sin(\Delta m\tau)}{\cosh(\frac{1}{2}\Delta\Gamma\tau) - \cos(\Delta m\tau)} \ . \end{aligned} \tag{14}$$

The use of these asymmetries is discussed in detail in the next section. The $\mathrm{K}^0_{\mathrm{e}3}$ form factor demands a somewhat different analysis [23], not reported in the present paper.

3 Experimental method

In the CPLEAR experiment, the neutral kaons were produced by antiproton annihilation at rest in a hydrogen target via the *golden* reactions

$$\overline{\mathrm{p}}\mathrm{p} \rightarrow \begin{array}{l}\mathrm{K}^-\pi^+\mathrm{K}^0 \\ \mathrm{K}^+\pi^-\overline{\mathrm{K}}^0\end{array} \ , \tag{15}$$

each having a branching ratio of $\approx 2 \times 10^{-3}$. The conservation of strangeness in the strong interaction dictates that a K^0 is accompanied by a K^-, and a $\overline{\mathrm{K}}^0$ by a K^+. Hence, the strangeness of the neutral kaon at production was tagged by measuring the charge sign of the accompanying charged kaon. If the neutral kaon subsequently decayed to $\mathrm{e}\pi\nu$, its strangeness could also be tagged at the decay time by the charge of the decay electron. Indeed, in the limit that only transitions with $\Delta S = \Delta Q$ take place, neutral kaons decay to e^+ if the strangeness is positive at the decay time and to e^- if it is negative.

For each initial strangeness, the number of neutral kaons decaying to $\mathrm{e}\pi\nu$, $N_+(\tau)$ and $\overline{N}_+(\tau)$ in the case of e^+, and $N_-(\tau)$ and $\overline{N}_-(\tau)$ in the case of e^-, were measured as a function of the decay time τ. These numbers were combined to form asymmetries, as in (14) – thus dealing mainly with ratios between measured quantities. However, the translation of measured numbers of events into decay rates requires (a) acceptance factors which do not cancel in the asymmetry, (b) residual background, and (c) regeneration effects to be taken into account.

(a) Detecting and strangeness-tagging neutral kaons at production and decay relied on measuring, at the production (primary) vertex, a $\mathrm{K}^\pm\pi^\mp$ track-pair, and the corresponding momenta $\vec{p}_{\mathrm{K}^\pm}$ and $\vec{p}_{\pi^\mp}$, and, at the decay (secondary) vertex, an $\mathrm{e}^\mp\pi^\pm$ track-pair, and the corresponding momenta $\vec{p}_{\mathrm{e}^\mp}$ and $\vec{p}_{\pi^\pm}$. The detection (tagging) efficiencies of the $\mathrm{K}^\pm\pi^\mp$ track-pairs depend on the pair charge configuration and momenta, and are denoted by $\epsilon(\vec{p}_{\mathrm{K}^\pm}, \vec{p}_{\pi^\mp})$, see Section 6.2. A similar dependence exists for the detection efficiencies of the $\mathrm{e}^\mp\pi^\pm$ track-pairs, $\epsilon(\vec{p}_{\mathrm{e}^\mp}, \vec{p}_{\pi^\pm})$, see Section 6.3. Since the detection efficiencies of primary and secondary track-pairs were mostly uncorrelated [1)], the acceptance of a signal ($\mathrm{e}\pi\nu$) event was factorized as $\varrho_S \times \epsilon(\vec{p}_{\mathrm{K}^\pm}, \vec{p}_{\pi^\mp}) \times \epsilon(\vec{p}_{\mathrm{e}^\mp}, \vec{p}_{\pi^\pm})$. The factor ϱ_S represents the portion of the acceptance which does not depend on the charge configuration of either primary or secondary particles. The acceptances of the events corresponding to different charge configurations were then equalized (or normalized) by introducing two functions:

$$\begin{aligned}\xi(\vec{p}_{\mathrm{K}}, \vec{p}_\pi) &\equiv \frac{\epsilon(\vec{p}_{\mathrm{K}^+}, \vec{p}_{\pi^-})}{\epsilon(\vec{p}_{\mathrm{K}^-}, \vec{p}_{\pi^+})}, \\ \eta(\vec{p}_{\mathrm{e}}, \vec{p}_\pi) &\equiv \frac{\epsilon(\vec{p}_{\mathrm{e}^-}, \vec{p}_{\pi^+})}{\epsilon(\vec{p}_{\mathrm{e}^+}, \vec{p}_{\pi^-})}.\end{aligned}$$

These functions, referred to as *primary-vertex normalization factor* and *secondary-vertex normalization factor*, respectively, are weights applied event by event, ξ to K^0 events and η to the events with a neutral kaon decaying to $\mathrm{e}^+\pi^-$.

[1)] see Section 6.4 for a discussion of this point.

(b) The background events consist of neutral-kaon decays to two or three pions with a pion misidentified as an electron, or decays to $e\pi\nu$ where the identities of the two charged particles are interchanged (see Section 6.5). Their number depends on the decay time τ and is important, with respect to the number of signal events, only for early decay times. To account for these events, the analytic expressions of the asymmetries, for example Eq. (14), were modified by adding to the rates $R_\pm$ and $\overline{R}_\pm$ the corresponding background rates $B_\pm$ and $\overline{B}_\pm$:

$$B_\pm(\tau) = \sum_i R_{Bi} \times \varrho_{Bi}/\varrho_S\,, \qquad \overline{B}_\pm(\tau) = \sum_i \overline{R}_{Bi} \times \varrho_{Bi}/\varrho_S\,, \tag{16}$$

where $R_{Bi}, \overline{R}_{Bi}$ are the rates of the background source i for initial K^0 and $\overline{\mathrm{K}}^0$, respectively, ϱ_S is defined above and ϱ_{Bi} is the corresponding term for the acceptance of events from the background source i. The quantities ϱ_{Bi} and ϱ_S were obtained by Monte Carlo simulation. Experimental asymmetries were formed from event rates including signal and background: $R^*_\pm = R_\pm + B_\pm$ and $\overline{R}^*_\pm = \overline{R}_\pm + \overline{B}_\pm$. These asymmetries were then fitted to the asymmetries of the *measured rates* (see below), which included residual background.

(c) The regeneration probabilities of K^0 and $\overline{\mathrm{K}}^0$ propagating through the detector material are not the same, thus making the measured ratio of initial $\overline{\mathrm{K}}^0$ to K^0 number of decay events at time τ different from that expected in vacuum. A correction was performed by giving each K^0 ($\overline{\mathrm{K}}^0$) event a weight w_r ($\overline{w}_r$) equal to the ratio of the decay probabilities for an initial K^0 ($\overline{\mathrm{K}}^0$) propagating in vacuum and through the detector, see Section 6.1.

Finally, each initial-K^0 event was given a total weight $w_+ = \xi \times \eta \times w_r$ or $w_- = \xi \times w_r$ if the final state was $\mathrm{e}^+\pi^-\nu$ or $\mathrm{e}^-\pi^+\overline{\nu}$, respectively. The summed weights in a decay-time bin are $N_{w+}(\tau)$ and $N_{w-}(\tau)$. In the same way, each initial-$\overline{\mathrm{K}}^0$ event was given a total weight $\overline{w}_+ = \eta \times \overline{w}_r$ or $\overline{w}_- = \overline{w}_r$ if the final state was $\mathrm{e}^+\pi^-\nu$ or $\mathrm{e}^-\pi^+\overline{\nu}$. The corresponding summed weights are $\overline{N}_{w+}(\tau)$ and $\overline{N}_{w-}(\tau)$. In the following $N_{w+}(\tau)$, $N_{w-}(\tau)$, $\overline{N}_{w+}(\tau)$ and $\overline{N}_{w-}(\tau)$ are referred to as the *measured decay rates*. From these we obtain the measured asymmetries considered in the present study:

$$A_{\mathrm{T}}^{\mathrm{exp}}(\tau) = \frac{\overline{N}_{w+}(\tau) - N_{w-}(\tau)}{\overline{N}_{w+}(\tau) + N_{w-}(\tau)}\,, \tag{17a}$$

$$A_{\delta}^{\mathrm{exp}}(\tau) = \frac{\overline{N}_{w+}(\tau) - \alpha N_{w-}(\tau)}{\overline{N}_{w+}(\tau) + \alpha N_{w-}(\tau)} + \frac{\overline{N}_{w-}(\tau) - \alpha N_{w+}(\tau)}{\overline{N}_{w-}(\tau) + \alpha N_{w+}(\tau)}\,, \tag{17b}$$

$$A_{\Delta m}^{\mathrm{exp}}(\tau) = \frac{[\overline{N}_{w-}(\tau) + \alpha N_{w+}(\tau)] - [\overline{N}_{w+}(\tau) + \alpha N_{w-}(\tau)]}{[\overline{N}_{w-}(\tau) + \alpha N_{w+}(\tau)] + [\overline{N}_{w+}(\tau) + \alpha N_{w-}(\tau)]}\,. \tag{17c}$$

The form of each of these asymmetries optimizes a specific measurement: $\mathcal{T}$ violation (Eq. 17a), $\mathcal{CPT}$ invariance (Eq. 17b) and Δm (Eq. 17c). The reason for the factor $\alpha = 1 + 4\mathrm{Re}(\varepsilon - \delta)$ will be discussed in Section 6.2. In order to extract the parameters of interest from each experimental asymmetry, we have to consider the corresponding phenomenological asymmetry functions:

$$A^*_{\mathrm{T}}(\tau) = \frac{\overline{R}^*_+(\tau) - R^*_-(\tau)}{\overline{R}^*_+(\tau) + R^*_-(\tau)}\,, \tag{18a}$$

$$A^*_{\delta}(\tau) = \frac{\overline{R}^*_+(\tau) - \alpha R^*_-(\tau)}{\overline{R}^*_+(\tau) + \alpha R^*_-(\tau)} + \frac{\overline{R}^*_-(\tau) - \alpha R^*_+(\tau)}{\overline{R}^*_-(\tau) + \alpha R^*_+(\tau)}\,, \tag{18b}$$

$$A^*_{\Delta m}(\tau) = \frac{[\overline{R}^*_-(\tau) + \alpha R^*_+(\tau)] - [\overline{R}^*_+(\tau) + \alpha R^*_-(\tau)]}{[\overline{R}^*_-(\tau) + \alpha R^*_+(\tau)] + [\overline{R}^*_+(\tau) + \alpha R^*_-(\tau)]}\,, \tag{18c}$$

for which explicit expressions will be given in Section 7.

4 The CPLEAR experiment

The main requirements affecting the design of the CPLEAR detector [24] were the following.

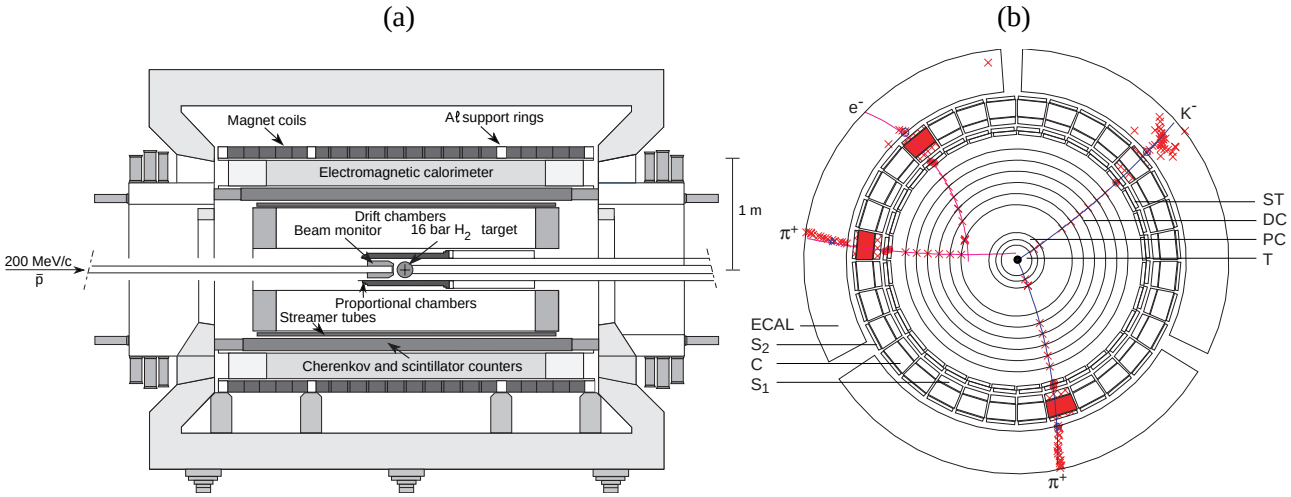

Figure 2: CPLEAR detector: (a) longitudinal view, and (b) transverse view and display of an event, $\overline{\mathrm{p}}\mathrm{p}$ (not shown) $\rightarrow \mathrm{K}^-\pi^+\mathrm{K}^0$ with the neutral kaon decaying to $\mathrm{e}^-\pi^+\overline{\nu}$. The view (b) is magnified twice with respect to (a) and does not show the magnet coils and outer detector components. In both views the central region refers to the early data taking without PC0.

- The selection of the $\overline{\mathrm{p}}\mathrm{p}$-annihilation channels of Eq. (15), and the determination of the neutral-kaon strangeness at the production vertex, by measuring the charge sign of the accompanying charged kaon. For this, fast and efficient identification of the charged kaon against a multipionic background was essential. Since Eq. (15) was observed at rest, the annihilation products were distributed isotropically, demanding a detector with a near-4π geometry.
- The identification of the neutral kaon's decay channel. The selection of $\mathrm{e}\pi\nu$ final states required to distinguish between pions and electrons.
- The measurement of the decay time, which was obtained as $\tau = m_{\mathrm{K}^0} \times d_{\mathrm{T}}/p_{\mathrm{T}}$. Here, m_{K^0} is the K^0 and $\overline{\mathrm{K}}^0$ average mass, d_{T} is the projection of the neutral-kaon path between production and decay vertices on a plane transverse to the magnetic field, and p_{T} is the transverse momentum component. Thus a high accuracy of the tracking system in the transverse plane was demanded.
- Decay-rate asymmetries must be formed for neutral-kaon decay times up to $\approx 20\ \tau_{\mathrm{S}}$. This set the size of the cylindrical K^0 decay volume to a radius of ≈ 60 cm.
- High statistics were necessary, which required high-rate capability and large geometrical coverage.
- Regeneration effects modify the time evolution of K^0 and $\overline{\mathrm{K}}^0$ differently, thus the amount of matter in the detector had to be minimized, especially in and around the target.

The detector and the trigger system are described in detail in Ref. [24]. For completeness, we summarize the detector characteristics in Section 4.1 and the trigger selection in Section 4.2.

4.1 Set-up

The Low Energy Antiproton Ring (LEAR) at CERN provided the antiprotons with a momentum of 200 MeV/c at a rate of $10^6\,\mathrm{s}^{-1}$ over an extraction period of ≈ 90 minutes. As shown in Fig. 2, the antiprotons entered the detector, where, after crossing a degrader and a 1-mm-scintillator beam counter, they were brought to rest and annihilated in a high-pressure gaseous hydrogen target. For data taken up to mid-1994 the target was a sphere of 7 cm radius at 16 bar pressure. Later, a cylindrical target with a 1.1 cm radius, at a pressure of 27 bar, was used. Around the new target a proportional chamber (PC0) was also installed. From 1995 onwards, it allowed a fast counting of charged tracks produced either in the annihilation process or in very early decays (mainly K_{S} to $\pi^+\pi^-$).

The detector had a cylindrical geometry and was mounted inside a solenoid of length 3.6 m and internal radius 1 m. The magnetic field of an intensity of 0.44 T was parallel, in the centre, to the antiproton beam. (The magnet centre was also the origin of the r, ϕ, z reference frame, with the z axis parallel to the magnet axis.)

The tracking of charged particles was performed with two layers of wires in the proportional chambers (PC1 and PC2), six drift chambers (DC1 to DC6) and two layers of streamer tubes (ST1 and ST2). The total material in the target and tracking chambers amounted to ≈ 300 mg·cm^{-2} and to $\approx 10^{-2}$ of equivalent radiation length (X_0). The r and $r\phi$ information from the PCs and DCs was used in the trigger for track finding and parametrization; the online z information was provided by the STs. After the track fit, the r and $r\phi$ resolutions were 350 μm and 300 μm for PCs and DCs, respectively, and the z resolution 2 mm. The momentum resolution of charged tracks, $\Delta p/p$, ranged from 5% to 10%, increasing with lifetime.

The charged kaon at the production vertex and the electron at the decay vertex were identified with the Particle Identification Detector (PID). The PID consisted of 32 trapezoidal sectors, each comprising a 3 cm thick inner scintillator (S1), a 8 cm thick threshold Cherenkov counter (C) and a 1.4 cm thick outer scintillator (S2), for a total of $0.5\,X_0$.

The Cherenkov radiator was liquid C_6F_{14} (Fluorinert FC72^{TM}), filling a 2 mm thick Plexiglas box. The radiator refractive index was 1.251, nearly independent of the wavelength. The Cherenkov light threshold was at a value of $\beta(\equiv v/c)$ close to 0.81: the β value of the highest-momentum kaons (< 800 MeV$/c$) after losing energy in S1.

The Cherenkov counter and the two scintillators were equipped with ADCs, and the inner scintillator also with TDCs. The TDCs measured the time interval (time of flight, TOF) between the beam counter signal ($t = 0$) and the S1 signal, with a resolution of 200 ps. Only TOF differences were used since absolute TOF measurements suffered from a spread of the annihilation times (with respect to the beam signal), owing to $\overline{\mathrm{p}}$ straggling in the target, from two to several nanoseconds . The ADCs measured the number of photoelectrons, N_{pe}, in the Cherenkov counter and the ionization energy loss, $\mathrm{d}E/\mathrm{d}x$, in the scintillators. The S1 resolution was twice as good as that for S2; the latter was mainly used to ensure that a charged particle had passed through the Cherenkov counter.

An electromagnetic calorimeter (ECAL), consisting of 18 layers of lead interleaved with high-gain streamer tubes, was used for photon detection and fast-electron identification. The calorimeter had a total thickness of $\approx 6\,X_0$.

4.2 Trigger and online selection

To cope with the high event rate and select the desired events from amongst the multipion annihilations, a multilevel trigger was designed and built. It was based on custom-made hardwired processors which identified the charged kaon and reconstructed the event kinematics in ≈ 6 μs. The overall rejection factor was ≈ 1000 before inserting PC0, and four times as much afterwards.

The trigger was initiated by a $\overline{\mathrm{p}}$ signal in the beam counter, separated in time from any other $\overline{\mathrm{p}}$ by more than 90 ns and in coincidence with a $\mathrm{S\overline{C}S}$ signal, that is with a coincidence of a S1 and a S2 signal not accompanied by a C signal. The mean probability that pions of momentum > 350 MeV$/c$ fake a $\mathrm{S\overline{C}S}$ signal was measured to be $< 6 \times 10^{-3}$. Owing to the small cell size of the drift chambers, the time separation of successive $\overline{\mathrm{p}}$ ensured a negligible probability of finding in the chambers track remnants from other annihilations.

The trigger system aimed to select the reactions of Eq. (15), regardless of the fate of the neutral kaon. It was split in six logical subsystems imposing the following requirements.

- Fast kaon: at least one kaon candidate, as indicated by a $\mathrm{S\overline{C}S}$ signal.
- PC0: no more than two hits in the proportional chamber PC0 (for data taken in 1995) to guarantee the decay of the neutral kaon away from the $\overline{\mathrm{p}}\mathrm{p}$ annihilation region.
- p_{T} cut: transverse momentum $p_{\mathrm{T}} > 300$ MeV$/c$ for the kaon candidate (thus removing low-momentum pions faking kaons). The p_{T} value was computed from the hit wires in DC1 and DC6, assuming that the track origin was at the centre of the target.
- Kinematics: two tracks originating at the centre of the detector (that is with PC hits) with opposite curvature (one of which was a kaon candidate) and with total momentum > 700 MeV$/c$.
- PID: for the kaon candidate, energy losses in S1 and S2, number of photoelectrons in C and time of flight must be consistent with the values expected for a kaon of the measured momentum.
- n_t : number of reconstructed tracks $n_t \geq 2$. (This is only a flag to filter offline at an early stage the events containing decays to charged final states: $n_t > 2$.)

The acceptances at these successive trigger levels are shown in Table 2 for multipion and multikaon $\overline{\mathrm{p}}\mathrm{p}$-annihilations (background), and for the golden events of Eq. (15) with a neutral kaon decaying to $\mathrm{e}\pi\nu$ or $\pi^+\pi^-$ within a radius of 45 cm [2]. We note that, despite the logic involving only the primary Kπ pair, the acceptance of golden events varies with the decay mode. The effect was traced back to the mode of operation of the trigger based on an 'OR' logic: an event was recorded if one combination of tracks fulfilled the trigger requirements, and the detection of primary and secondary pairs could then be correlated. Offline, only events not showing such correlation were selected, see Section 5.3.

From 1992 to 1995, about 10^{13} $\overline{\mathrm{p}}$ were delivered to the experiment and 5×10^9 events were recorded on tape (raw data). There were about the same number of events for opposite magnetic-field polarities. For calibration purposes, a small percentage of these was recorded with a minimum-bias trigger (T1). This trigger required only the coincidence of the beam counter and an S1 signal, and accepted events in the entire phase space, limited only by the energy thresholds and geometrical acceptances. The T1 trigger operated at regular intervals of about eight hours, before and after changing the magnetic-field polarity.

Table 2: Acceptances at various trigger levels for background (multipion or multikaon $\overline{\mathrm{p}}\mathrm{p}$-annihilation events) and signal (golden events with neutral kaon decaying to $\mathrm{e}\pi\nu$ or $\pi^+\pi^-$).

	multipion background	multikaon background	Golden: $\mathrm{e}\pi\nu$	Golden: $\pi^+\pi^-$
Fast kaon	0.19	0.34	0.39	0.43
PC0	0.054	0.15	0.36	0.19
p_{T} cut	0.011	0.092	0.24	0.13
Kinematics	0.0051	0.046	0.15	0.092
PID	2.7×10^{-4}	0.016	0.10	0.056
$n_t > 2$	2.8×10^{-5}	0.001	0.081	0.053

5 Event selection (offline) and comparison with simulated data

The selection of the signal events (golden reaction followed by neutral-kaon decay to $\mathrm{e}\pi\nu$) was performed offline by a set of topological cuts and constrained fits. The same cuts were applied to both real and simulated data. The latter, owing to the high statistics (larger than the data sample by one order of magnitude) allowed precise monitoring of efficiencies and losses in all selections. The data reduction proceeded through three main steps (roughly a factor of hundred, ten and five). Through the same analysis, the number of simulated $\mathrm{e}\pi\nu$ events was reduced by about a factor of ten. The background reduction factor was of the order of 10^5.

5.1 Topological filter and constrained fits (a)

In the offline procedure, the signals from each subdetector were first decoded and translated into physical quantities, like the space coordinates of track hit-points, the number of photoelectrons in the Cherenkov counter, or the energy-loss in each scintillator. Information from initial surveys and successive calibrations, regularly interleaved with data collection (see above), was used for this purpose.

Pattern recognition and track fit were performed: 68% of the events contained two (22%) or four (46%) tracks of good quality. Of these one was a kaon candidate, and two or more were primaries, i.e. containing at least one PC hit. Back-scattered tracks (present in a few percent of the events and mainly originating in the calorimeter) were not validated by the pattern recognition. For 90% of the four-track events the momentum, the charge, a reference point in space and the χ^2 of the fit were determined for all the tracks. Vertices were sought, including a primary vertex inside the target. Tracks with a momentum $< 60\ \mathrm{MeV}/c$ (which would not reach S1) or $> 1\ \mathrm{GeV}/c$ (which would not be produced in a $\overline{\mathrm{p}}\mathrm{p}$ annihilation) were discarded. Of the four-track events, 64% had primary-pair momenta fitted by Eq. (15) with a 1C-fit probability $> 2.5\%$, and 24% also had secondary-pair momenta fitted by a neutral-kaon decay to $\pi^+\pi^-$ (the vast majority) or to $\mathrm{e}\pi\nu$.

[2] The fiducial volume has a radius of 45 cm: it contains 3% of the $\mathrm{K_L}$ decay vertices.

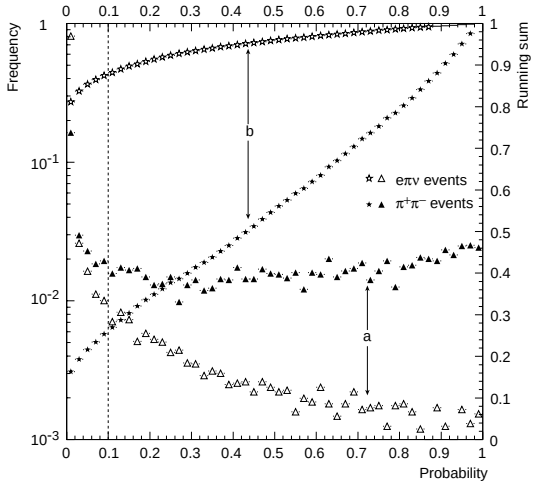

Figure 3: Simulated $\mathrm{e}\pi\nu$ and $\pi^+\pi^-$ events fitted with the $\pi^+\pi^-$ hypothesis: 4C-fit probability. Distributions of (a) relative-frequency density and (b) relative-frequency running sum. The dotted line indicates the cut position.

The topology of an $\mathrm{e}\pi\nu$ event was then defined by the following criteria, which tightened the cuts mentioned above.

- The event contained four charged tracks. All the tracks passed through different S1 sectors. Each primary (secondary) track had at least five (four) hits in the tracking chambers and each track had at least two hits in the longitudinal plane. The reduced χ^2 of the track fit was $\chi^2/\mathrm{ndf} < 5$. The probability for the four tracks to originate from the same vertex was $< 5\%$.
- At least one of the four tracks had a $\mathrm{S\overline{C}S}$ signature and was a charged-kaon candidate (see Section 4.2). Its transverse momentum p_T was larger than 300 MeV/c and its total momentum p larger than 350 MeV/c. Its $\mathrm{d}E/\mathrm{d}x$ and $\mathrm{d}N_{pe}/\mathrm{d}x$ were within three standard deviations from the expected values.
- The kaon-candidate track intersected an opposite-charge track at a primary vertex V1 within the target volume ($r_{V1} < 1$ cm and $|z_{V1}| < 3$ cm). The track with the same charge sign as the 'kaon' intersected the remaining opposite-sign track at a secondary vertex V2. The primary and secondary vertices were separated by more than 1 cm in the transverse plane ($r_{V2} > 1.7$ cm if the trigger included the PC0 information). The secondary vertex also satisfied $r_{\mathrm{V2}} < 36$ cm, $|z_{\mathrm{V2}}| < 40$ cm to ensure secondary tracks of sufficient length.
- The opening angle between any two intersecting tracks was in the interval $11^\circ - 169^\circ$. Events with tracks almost parallel or back-to-back were removed as they have a poorly defined vertex position. Most events containing photon conversions were removed by this selection.
- The momenta of the primary track pair were fitted by Eq. (15) with a 1C-fit probability $> 2.5\%$. This imposed the constraint that the missing mass at the primary vertex was equal to the neutral-kaon mass.

In addition, an overall four-momentum conservation was imposed to the event. This meant a 4C fit with the hypothesis that the decay be to $\pi^+\pi^-$, and a 1C fit with the $\mathrm{e}\pi\nu$ hypothesis. The $\mathrm{e}\pi\nu$ fit became a 2C fit by adding the constraint that the missing mass at the primary vertex be equal to the neutral-kaon mass. The results were as follows.

- Under the hypothesis of decay to $\pi^+\pi^-$, events with a 4C-fit probability $> 10\%$ were rejected, removing 75% of $\pi^+\pi^-$ events and keeping 88% of $\mathrm{e}\pi\nu$ events, see Fig. 3. This fit reduced the $\mathrm{K}^0(\overline{\mathrm{K}}^0) \to \pi^+\pi^-$ background dominant at early decay times.
- Under the hypothesis of decay to $\mathrm{e}\pi\nu$, events with a 2C-fit probability $> 5\%$ for at least one combination of tracks were accepted.

Better selection of the $\mathrm{e}\pi\nu$ events needed electron selection, which is specific to the present analysis, see Section 5.2. Firstly, the following criterion was applied.

- Events where both secondary tracks had a probability $> 4\%$ of being a pion were rejected.

With the set of criteria listed under (•) the number of $\mathrm{e}\pi\nu$ candidates was reduced by a factor of ten.

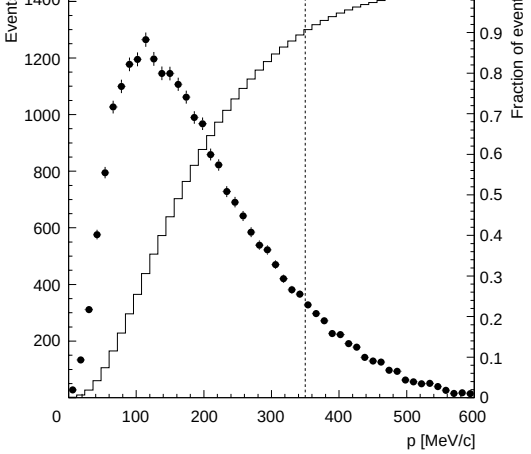

Figure 4: Simulated neutral-kaon decays to $\mathrm{e}\pi\nu$: electron momentum p. Distributions of frequency density (•) and relative-frequency running sum (continuous line). The dotted line indicates the cut position.

5.2 Electron/pion separation – PID neural network

Figure 4 shows the electron-momentum spectrum at the decay vertex, as given by the simulation (vector interaction [25] and a form-factor slope $\lambda_+ = 0.03$ [7] were assumed to model the momentum dependence of the decay amplitude). In 90% of the decays the electron momentum p_e was $< 350\ \mathrm{MeV}/c$, with the distribution peaking at $115\ \mathrm{MeV}/c$.

At these momenta the differences in β between pions and electrons could be exploited by using the PID information together with the measured momentum of the particle. Thus, six parameters were determined for each secondary track (see Fig. 5):

- the momentum p, computed by the track fit;
- the energy loss per cm, $\mathrm{d}E/\mathrm{d}x$, in the scintillator S1;
- the number of photoelectrons per cm, $\mathrm{d}N_{pe}/\mathrm{d}x$, in the Cherenkov counter C;
- the energy loss per cm, $\mathrm{d}E/\mathrm{d}x$, in the scintillator S2;
- the difference between the measured TOF of the particle and the expected one if it was a pion;
- the difference between the measured TOF of the particle and the expected one if it was an electron.

At momenta above $350\ \mathrm{MeV}/c$, the electrons could have been identified using the calorimeter information [27]. However, because of the energy loss in the PID ($\approx$ 40 MeV for minimum ionizing particles) only electrons with $p_\mathrm{e} > 200\ \mathrm{MeV}/c$ were detected in the calorimeter with full efficiency. To preserve the homogeneity of the analysis, we chose not to use the calorimeter data. At the cost of a small loss in statistics, only events with an electron momentum $p_\mathrm{e} < 350\ \mathrm{MeV}/c$ were considered. For these events the electron identification relied on the PID 6-dimensional information. This demanded a set of calibrations and was best analysed using a neural network (NN) algorithm [28]. As a first step, the Cherenkov response of a prototype sector was studied in a beam at the Paul-Scherrer-Institute (PSI) cyclotron, with electrons, muons and pions, as a function of momentum, impact point in the radiator, and beam angle with respect to the Cherenkov counter. Figure 6 shows typical photoelectron yields. Of these, only the muon dependence on momentum agreed with the expectation. The electron large signal pointed to δ-ray production and electromagnetic showering. The pion response, hampered by strong interactions, led to a signal at momenta below threshold ($180\ \mathrm{MeV}/c$).

In practice, the PID response to electrons and pions was measured for identified samples of particles collected using the full set-up. In dedicated runs $\overline{\mathrm{p}}\mathrm{p}$ annihilations to $\pi^+\pi^-\mathrm{n}\pi^0$ ($\pi^0 \to 2\gamma$) or to $2\pi^+2\pi^-$ were selected to provide kinematically identified pions and electrons in the momentum range $50 - 350\ \mathrm{MeV}/c$ ($\mathrm{e}^+\mathrm{e}^-$ pairs originating from photon conversion had a clean signature, characterized by an opening angle close to 0°).

The NN algorithm was optimized using these measured responses. For each track in the momentum range $50 - 350\ \mathrm{MeV}/c$, the NN output yielded a parameter x_N between 0 and 1. Electrons cluster at small x_N values, pions at large x_N. The probability for the track to be an electron, $\mathcal{P}_\mathrm{e}$, was defined as the fraction of the electron distribution lying below that value of x_N. The probability to be a pion, $\mathcal{P}_\pi$, was

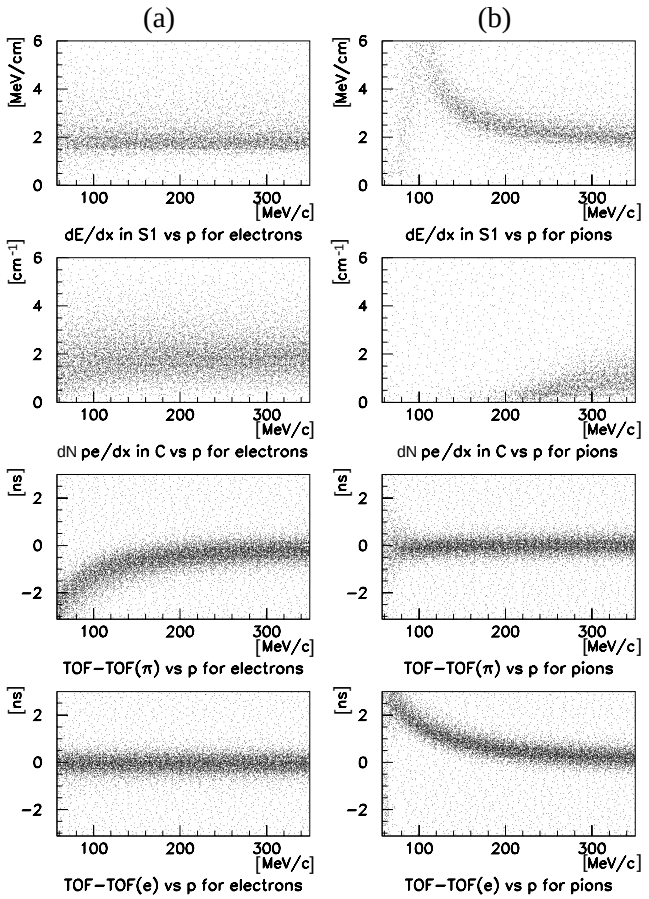

Figure 5: The response of the Particle Identification Detector to (a) electrons and (b) pions as a function of momentum p: $\mathrm{d}E/\mathrm{d}x$ in the scintillator S1, $\mathrm{d}N_{pe}/\mathrm{d}x$ in the Cherenkov counter C, and $\Delta(\mathrm{TOF})$. The last quantity is the difference between the measured and expected time of flight, $\mathrm{TOF(e)}$ or $\mathrm{TOF}(\pi)$ assuming the particle to be an electron or a pion.

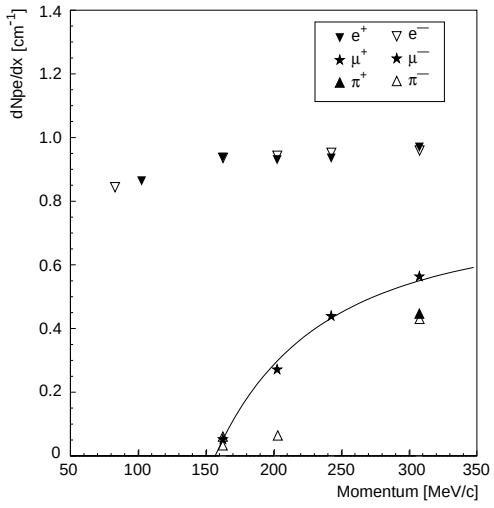

Figure 6: $\mathrm{d}N_{pe}/\mathrm{d}x$ for positive and negative particles in the prototype Cherenkov counter as a function of momentum. The continuous line is the result of the fit with the expected muon yield.

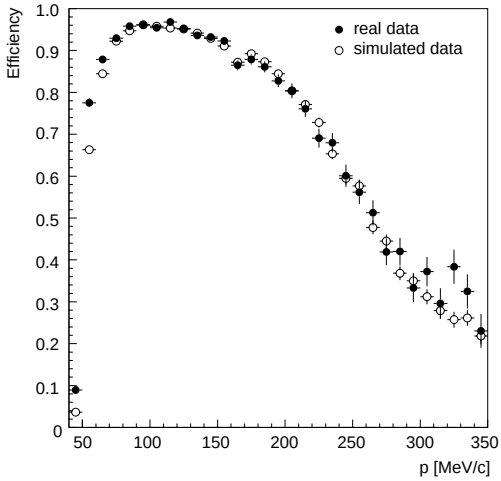

Figure 7: Electron identification efficiency as a function of momentum when $< 2\%$ of pions fake electrons, for real (●) and simulated (○) calibration data.

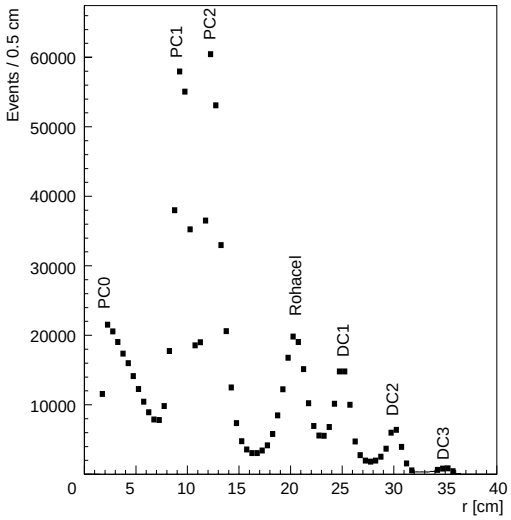

Figure 8: Radial distribution of $\mathrm{e^+e^-}$ vertices ($\mathrm{K^0} \to \pi^0\pi^0$ real data). The concentration of matter in the wire chambers (PCs and DCs) and in the Rohacel$^{\mathrm{TM}}$ entrance window of the DCs is clearly visible. The enhancement at short radii originates from $\pi^0 \to \gamma\mathrm{e^+e^-}$ Dalitz decays.

defined as the fraction of the pion distribution lying above x_{N}. For the final selection (Section 5.3) a track was defined to be an electron if $\mathcal{P}_{\mathrm{e}} > 0$ and $\mathcal{P}_{\pi} < 0.02$. A non-electron track was defined to be a pion. No attempt was made to identify muons with NN (decays to $\mu\pi\nu$ are considered in Section 6.5). Figure 7 shows the identification efficiency for real and simulated electrons of the calibration samples when $< 2\%$ pion background was allowed. The good agreement between the two sets of data was expected since only electromagnetic processes were involved.

During data taking, the quality of the NN response was verified with electron and pion samples obtained with the current trigger. Pairs of $\mathrm{e^+e^-}$ from γ conversions in the detector materials were selected from neutral-kaon decays to $\pi^0\pi^0$ (Tγ sample). Figure 8 shows the radial distribution of the $\mathrm{e^+e^-}$ vertices. Charged pions were obtained from neutral-kaon decays to $\pi^+\pi^-$ at early decay times, selected with negligible background in the standard $\pi^+\pi^-$ analysis [29].

5.3 Topological filter and constrained fits (b)

If one and only one of the secondary tracks was recognized as an electron by the NN, a 6C fit was performed with the hypothesis of a decay to $\mathrm{e}\pi\nu$. The kinematic constraints of the 2C fit (Section 5.1) were used together with geometric constraints – the neutral-kaon momentum had to be parallel to the vector joining the primary and secondary vertex, and at each vertex the two tracks must coincide in z.

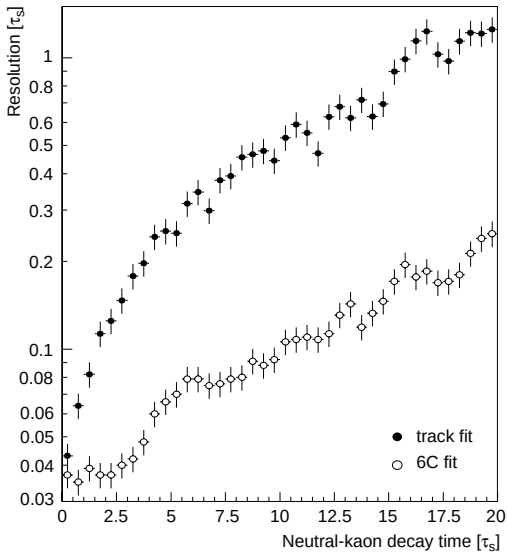

Figure 9: Decay-time resolutions after track fit (●) and 6C fit (○), as a function of the decay time.

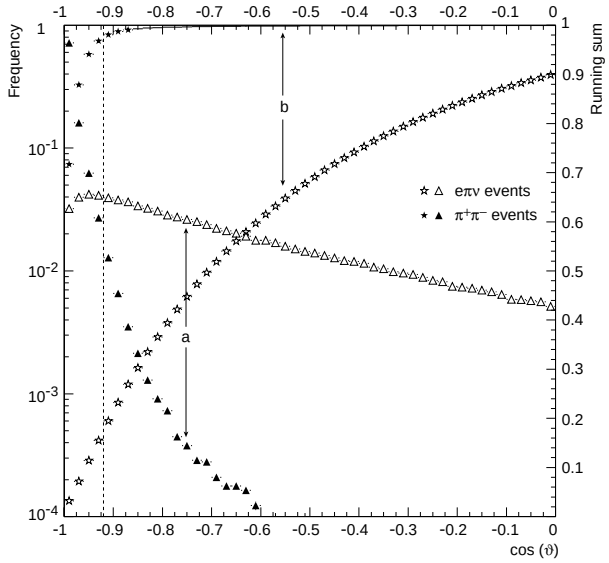

Figure 10: Simulated $e\pi\nu$ and $\pi^+\pi^-$ events fitted with the $e\pi\nu$ hypothesis : $\cos(\vartheta)$, $\vartheta \equiv$ opening angle between electron and pion momentum in the K^0 rest frame. Distributions of (a) relative-frequency density and (b) relative-frequency running sum. The dotted line indicates the cut position.

Events with a 6C-fit probability $> 5\%$ and only one good configuration were kept. The momenta and vertices resulting from this fit determined the decay time. The decay-time resolution was computed from the simulated sample. Figure 9 shows that it increases from 0.04 τ_S to 0.3 τ_S going from early to late decay times.

On the events selected, a further kinematic cut was applied, based on the opening angle, ϑ, of the two charged secondaries in the rest frame of the neutral kaon. As shown in Fig. 10, the distributions of $\cos(\vartheta)$ are different for decays to $e\pi\nu$ and to $\pi^+\pi^-$. Rejecting events with $\cos(\vartheta) < -0.92$ decreased the amount of $\pi^+\pi^-$ background by a factor 20, while only 15% of $e\pi\nu$ events were lost.

The next cut did not aim at a better selection of $e\pi\nu$ events as such, but was essential in order to avoid biases when forming decay-rate asymmetries, see Section 6.2. The charged kaon and associated (primary) pion, found in the offline analysis, must be the same tracks as those used online to satisfy the trigger conditions at each stage (the trigger could have seen a secondary particle as one of the primaries, mainly if the secondary vertex was at a radius smaller than the PC2 radius). This *trigger matching* ensured that no event entered the final sample if the trigger conditions were satisfied by tracks other than the *true* primary $K\pi$ pair. For that purpose the events were filtered through the trigger simulation, either using

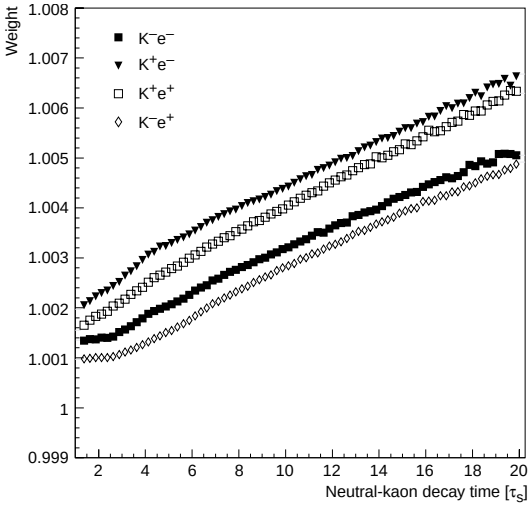

Figure 11: Regeneration weights for $\mathrm{e}\pi\nu$ events (averaged over the neutral-kaon momenta between 550 and 650 MeV/c) as a function of the decay time for the four possible combinations of charge signs of kaon (initial state) and electron (final state).

the detector raw data, or else the corresponding online information. About 10% of the events were thus removed from the final sample. As a result, the ratio between the acceptances of events originating from initial $\overline{\mathrm{K}}^0$ and K^0 became largely uncorrelated with the final-state topology (see Section 6.2).

At the end of the offline analysis, we obtained a total of 1.3×10^6 events with a measured decay time $> 1\ \tau_\mathrm{S}$. This number reduced to 1.2×10^6 in the case of the $A_{\Delta m}$ asymmetry because of two more cuts (to be discussed in Section 7.4). The corrections (or weights) which need to be applied to the measured numbers of initial K^0 and $\overline{\mathrm{K}}^0$ events prior to forming the asymmetries of Eqs. (17), and the determination of the residual background level, are discussed in Section 6.

6 Decay-rate corrections and background evaluation

6.1 Regeneration

The measured numbers of initial K^0 and $\overline{\mathrm{K}}^0$ decaying to $\mathrm{e}\pi\nu$ must be corrected for both coherent and incoherent regeneration effects. These arise because the neutral-kaon scattering off the nuclei of the detector material depends on the strangeness of the incoming particle, thereby altering the corresponding $\mathrm{K_S}$ and $\mathrm{K_L}$ mixing. The correction was performed by giving each event a weight, equal to the ratio of the initial K^0, or $\overline{\mathrm{K}}^0$, decay probability when propagating in vacuum to that when traversing the detector. This ratio depends on the initial strangeness of the neutral kaon, on the charge of the decay electron, on the magnitude and direction of the neutral-kaon momentum, and on the position of its production and decay vertices. The calculation of the correction required an accurate description of all the detector materials traversed by the neutral kaon and the knowledge of the difference Δf between the forward-scattering amplitudes of K^0 and $\overline{\mathrm{K}}^0$, which is momentum dependent. During dedicated data-taking in 1996, a carbon regenerator was inserted into the detector, enabling us to measure these amplitudes [30]. The measured values were in good agreement with earlier calculations and allowed the systematic error on the size of the regeneration correction to be reduced. Figure 11 shows for the cylindrical (thinner) target the distribution of the weights versus decay time, for neutral-kaon momenta between 550 and 650 MeV/c. The $\mathrm{e}\pi\nu$ weights are smaller than or of the same order as the weights used in the $\pi^+\pi^-$ analysis. The relative difference between K^0 and $\overline{\mathrm{K}}^0$ event weights, all other conditions being the same, stays within 0.2% for the same electron charge in the final state, and is even smaller when we compare the weights of either K^0 or $\overline{\mathrm{K}}^0$ with opposite-charge electrons in the final state.

The overall effect of the coherent regeneration correction in the $\mathrm{e}\pi\nu$ analysis is in general small, compared to the statistical error of the various parameters, see Section 7. The effect of incoherent regeneration is even smaller, and may safely be neglected.

6.2 Primary-vertex normalization

As mentioned in Section 3, the detection efficiencies of the primary $\mathrm{K}^{\mp}\pi^{\pm}$ pairs, used to tag K^0 and $\overline{\mathrm{K}}^0$ production, were not the same. The difference resulted from two sources.

- Slight geometrical imperfections in the detector which cause the detection efficiency of a track to depend on its curvature sign. This also arises from biases introduced by the trigger, which assumes, for example, that all particles originate from the centre of the detector.
- Differences in the strong interaction cross sections of K^+ and K^-, and of π^+ and π^-, with the detector material (principally the scintillators and Cherenkov counter).

Neither of the above effects could be modelled with sufficient accuracy to determine the efficiencies ratio, ξ, from simulated data. However, ξ is also the ratio of the acceptances of initial $\overline{\mathrm{K}}^0$ and K^0 decaying to $\pi^+\pi^-$ (the efficiency of detecting a $\pi^+\pi^-$ pair is the same for a K^0 or a $\overline{\mathrm{K}}^0$ decay). Since ξ is independent of the decay mode (see Section 5.3) it was possible to determine it from neutral-kaon decays to $\pi^+\pi^-$. For that purpose, we used events recorded in the same experiment [29] in a decay-time interval between 1 and 4 τ_{S}, where statistics were high, the proportion of background events was negligible (see Section 6.3) and $\mathcal{CP}$-violation effects were small. This method allowed us to take into account all the online and the offline biases which affect ξ.

In the range of decay times considered, for a bin of primary $\mathrm{K}^{\pm}\pi^{\mp}$ kinematic configurations, $\vec{p}_{\mathrm{K}}, \vec{p}_{\pi}$, we obtain for Eq. (13), denoting by N_1 and $\overline{N}_1$ the summed regeneration weights of K^0 and $\overline{\mathrm{K}}^0$ decays to $\pi^+\pi^-$,

$$\begin{aligned}\frac{R_f(\tau)}{\overline{R}_f(\tau)} &= \xi(\vec{p}_{\mathrm{K}},\vec{p}_{\pi})\frac{N_1(\tau|\,\vec{p}_{\mathrm{K}},\vec{p}_{\pi})}{\overline{N}_1(\tau|\,\vec{p}_{\mathrm{K}},\vec{p}_{\pi})} \\ &\approx \frac{[1-2\mathrm{Re}(\varepsilon-\delta)]\big(1+2|\eta_{+-}|\mathrm{e}^{\frac{1}{2}\Gamma_{\mathrm{S}}\tau}\cos(\Delta m\tau-\phi_{+-})\big)}{[1+2\mathrm{Re}(\varepsilon-\delta)]\big(1-2|\eta_{+-}|\mathrm{e}^{\frac{1}{2}\Gamma_{\mathrm{S}}\tau}\cos(\Delta m\tau-\phi_{+-})\big)} = \frac{1-4\mathrm{Re}(\varepsilon-\delta)}{1-f(\tau)}\,,\end{aligned}$$

where terms $\propto |\eta_{+-}|^2$, and $\Gamma_{\mathrm{L}} \ll \Gamma_{\mathrm{S}}$ are neglected, and $f(\tau) = 4|\eta_{+-}|\mathrm{e}^{\frac{1}{2}\Gamma_{\mathrm{S}}\tau}\cos(\Delta m\tau-\phi_{+-})$ remains < 0.03 and is known with an error of a few times 10^{-4} (in this decay-time range and using world-average values [26] for the relevant parameters). Summing over all the decay times between 1 and 4 τ_{S}, we have

$$\begin{aligned}\alpha\xi(\vec{p}_{\mathrm{K}},\vec{p}_{\pi}) &\equiv [1+4\mathrm{Re}(\varepsilon-\delta)]\xi(\vec{p}_{\mathrm{K}},\vec{p}_{\pi}) \\ &= \frac{\sum \overline{N}_1(\tau|\,\vec{p}_{\mathrm{K}},\vec{p}_{\pi})}{\sum N_1(\tau|\,\vec{p}_{\mathrm{K}},\vec{p}_{\pi})\big(1-f(\tau)\big)}\,. \end{aligned} \tag{19}$$

Figure 12 shows the projections of $\alpha\xi$ onto three kinematic variables, the transverse and longitudinal components of the charged-kaon momentum, p^t_{K} and p^{ℓ}_{K}, and the magnitude of the pion momentum, p_{π}, for each polarity of magnetic field. Differences arising from curvature-dependent efficiencies are clearly visible. Figure 13 displays $\alpha\xi$ when K^0 and $\overline{\mathrm{K}}^0$ events entering the ratio were measured with magnetic fields of opposite polarities, so that the charged kaons (and the corresponding pions) have the same curvature sign. Figure 13 suggests how these biases could be eliminated by adding the data from the two field polarities. This was confirmed by studies using high-statistics, simulated data. Thus under steady data-taking conditions, the polarity was reversed every eight hours and equal amounts of data were taken with each field polarity. They were then summed up to form the K^0 and $\overline{\mathrm{K}}^0$ data samples to which we refer in the following.

Equivalent information is contained in the $\alpha\xi$ dependence on the neutral-kaon transverse momentum p_{T} (correlated to p^t_{K}, p^{ℓ}_{K} and p_{π}), see Fig. 14 and Ref. [29]. In addition, this figure suggests a dependence of ξ on the neutral-kaon decay time, owing to the correlation between momentum and decay time, which, in turn, is a consequence of the finite decay volume of the detector: those neutral kaons with high momentum decaying on average at earlier times than those with low momentum.

Finally, a multi-dimensional table of event weights was constructed. These weights consisted of the quantities $\alpha\xi$ determined from Eq. (19) in bins of the primary $\mathrm{K}^{\pm}\pi^{\mp}$ variables, and were applied to the K^0 decays on an event-by-event basis. This is the reason for the explicit appearance of the factor α

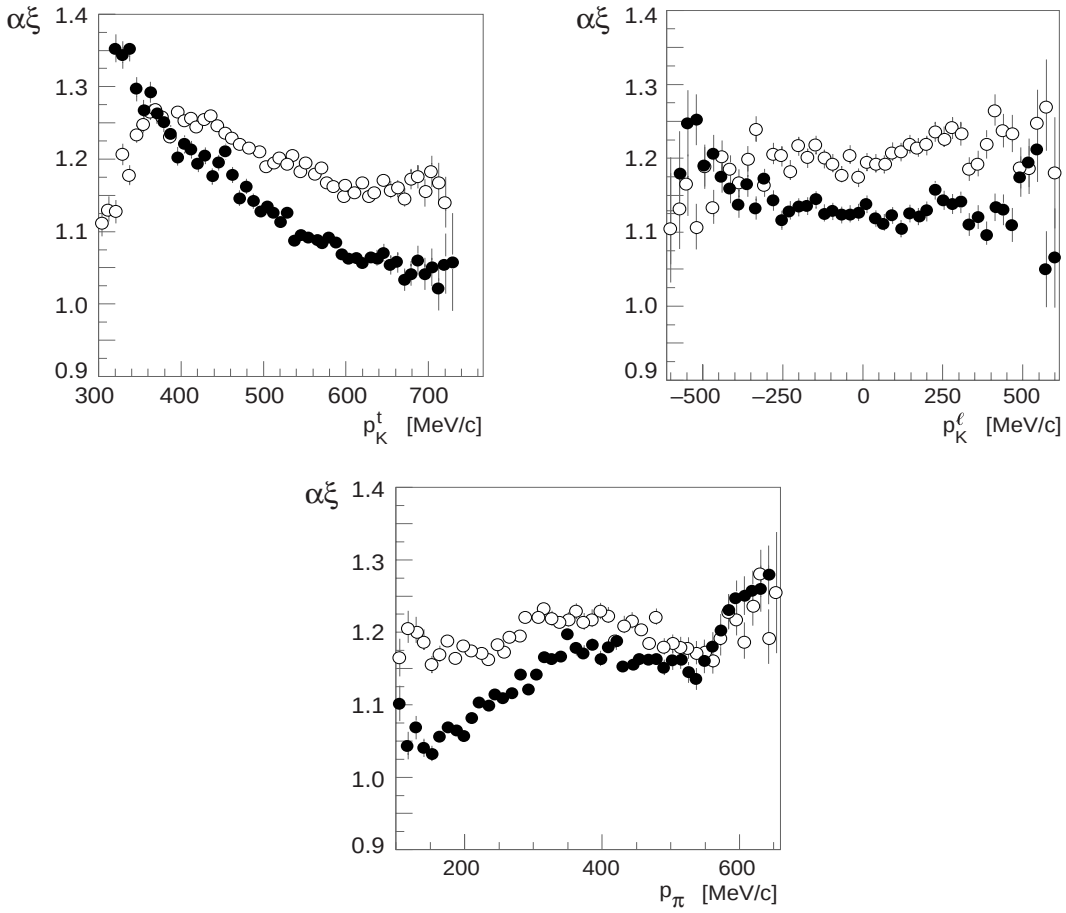

Figure 12: The projection of $\alpha\xi$ onto the transverse and longitudinal components of the charged-kaon momentum, $p_{\rm K}^t$ and $p_{\rm K}^\ell$, and onto the primary-pion momentum, p_π, for positive (•) and negative (○) polarity of the magnetic field.

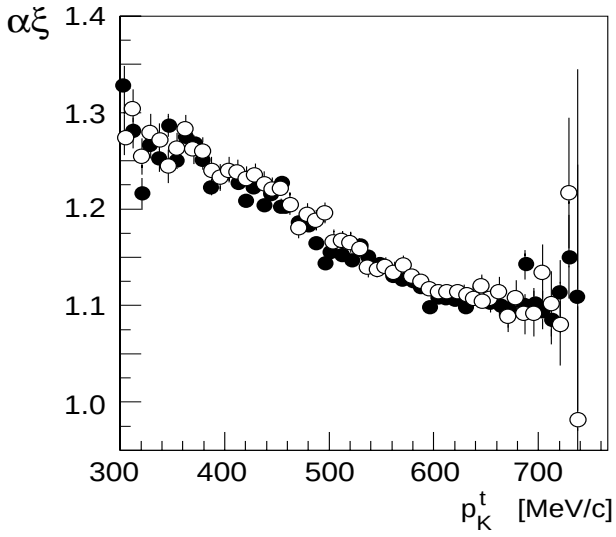

Figure 13: The projection of $\alpha\xi$ onto the transverse component of the charged-kaon momentum $p_{\rm K}^t$, for events with positive (○) and negative (•) curvature, see text.

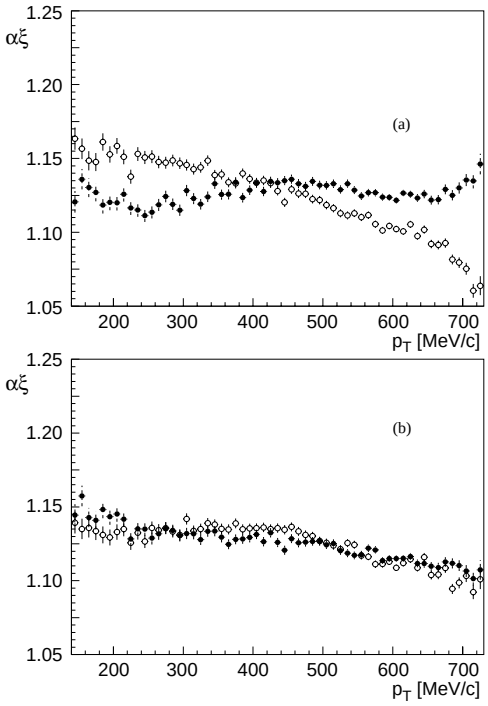

Figure 14: The projection of $\alpha\xi$ onto the neutral-kaon transverse momentum p_{T}, when (a) K^0 and $\overline{\mathrm{K}}^0$ events are measured with the same magnetic-field polarity, positive (○) or negative (●), and (b) K^0 and $\overline{\mathrm{K}}^0$ events are measured with opposite field polarities, so that the charged kaons have the same curvature sign, positive (○) or negative (●).

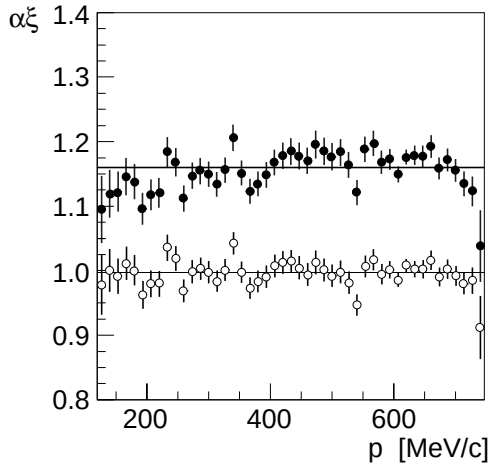

Figure 15: Primary-vertex normalization $\alpha\xi$ for simulated $\mathrm{e}\pi\nu$ events before (●) and after (○) the weighting procedure as a function of neutral-kaon momentum p. The continuous lines are the results of a fit with a constant.

multiplying the summed K^0 weights in Eqs. (17b-c). In practice, it was adequate to produce the table of event weights in only a subset of the $\mathrm{K}^{\pm}\pi^{\mp}$ variables, namely transverse and longitudinal components of the charged-kaon momentum, p_{K}^t (in bins of 20 MeV/c) and p_{K}^{ℓ} (in bins of 120 MeV/c), and magnitude of the primary-pion momentum p_π (in bins of 56 MeV/c). The validity of the method was verified for the present $\mathrm{e}\pi\nu$ analysis with simulated data (with weights obtained by simulation of the $\pi^+\pi^-$ channel). As an example, Fig. 15 shows the quantity $\alpha\xi$ for the $\mathrm{e}\pi\nu$ simulated sample as a function of the neutral-kaon momentum before and after the weighting procedure. We note that the term $4\mathrm{Re}(\varepsilon-\delta)$ contained in α has no impact on the phenomenological expressions corresponding to the asymmetries of Eqs. (17b-c). It cancels altogether in the A_δ^* asymmetry, Eq. (18b) and Section 7.5, and to first order in the $A_{\Delta m}^*$ asymmetry, Eq. (18c) and Section 7.4.

The case of the asymmetry $A_{\mathrm{T}}^{\mathrm{exp}}$ in Eq. (17a) is different: the weights $\alpha\xi$, obtained from the $\pi^+\pi^-$ analysis as mentioned above, had to be divided by α before applying them event-by-event. In order to evaluate $4\mathrm{Re}(\varepsilon-\delta)$, we made use of the relation [22]:

$$2\mathrm{Re}(\varepsilon-\delta)=\delta_\ell+2(\mathrm{Re}(x_-)\ +\mathrm{Re}(y)). \tag{20}$$

Here δ_ℓ is the $\mathrm{K_L}$ (measured) charge asymmetry for which we assumed the world-average value $\delta_\ell = (3.27\pm0.12)\times10^{-3}$ [26]. Since the quantity $2(\mathrm{Re}(x_-)\ +\mathrm{Re}(y))$ was not known, the weights obtained from the $\pi^+\pi^-$ analysis were simply divided by $(1+2\delta_\ell)$, and a term $-2(\mathrm{Re}(x_-)\ +\mathrm{Re}(y))$ was added to the phenomenological expression of this asymmetry, see Section 7.6. We note, however, that in the limit of $\mathcal{CPT}$ invariance in neutral-kaon decay to $\mathrm{e}\pi\nu$, $\mathrm{Re}(x_-)=\mathrm{Re}(y)=\ 0$. In the same limit the ξ average value over the $\mathrm{e}\pi\nu$ data-set was evaluated to be $\langle\xi\rangle=\langle\alpha\xi/(1+2\delta_\ell)\rangle=1.12023\ \pm\ 0.00043$.

6.3 Normalization of e^+ and e^- final states

As mentioned in Section 3, each neutral-kaon decay to $\mathrm{e}^+\pi^-\nu$ needed to be weighted with a quantity $\eta=\epsilon(\vec{p}_{\mathrm{e}^-},\vec{p}_{\pi^+})/\epsilon(\vec{p}_{\mathrm{e}^+},\vec{p}_{\pi^-})$, that is the ratio of the charged-pair acceptances at the decay vertex. In contrast to ξ, the ratio of the charged-pair acceptances at the production vertex, η, could not be determined in a unique calibration process. A detailed analysis of all levels of the experiment was therefore necessary, from detection processes and online requirements, to offline criteria.

This analysis was performed using real data: a sample of 3×10^4 $\mathrm{e}^+\mathrm{e}^-$ pairs with a pion contamination $<2\%$, obtained from the Tγ data of Section 5.2, and pions from the minimum-bias T1 sample. The T1 data were selected offline so as to have a clean sample of 2×10^5 $\overline{\mathrm{p}}\mathrm{p}$ annihilations to four charged pions (the 4C-fit probability with that hypothesis was >0.05). For the simulation we made use of the high-statistics T23 sample: $\overline{\mathrm{p}}\mathrm{p}\to\mathrm{K}^{\pm}\pi^{\mp}\overline{\mathrm{K}}^0(\mathrm{K}^0)$ events with a charged-kaon of conveniently large p_{T}, where the neutral kaon was let to decay to $\pi^+\pi^-$ or $\pi^0\pi^0$.

To start with, η was assumed to be only dependent on p_{e} and p_π and factorized as follows:

$$\eta(p_{\mathrm{e}},p_\pi)=\eta_{\mathrm{S1}}(p_{\mathrm{e}},p_\pi)\times\eta_{\mathrm{OL}}(p_{\mathrm{e}},p_\pi)\times\eta_{\mathrm{NN}}(p_{\mathrm{e}})\,, \tag{21}$$

where $\eta_{\mathrm{S1}}=\eta(p_{\mathrm{e}},p_\pi|\mathrm{S1})$ accounts for the different probabilities that electrons or pions of opposite charge have to give a signal in the scintillator S1; $\eta_{\mathrm{OL}}=\eta(p_{\mathrm{e}},p_\pi|\mathrm{OL})$ parametrizes any additional acceptance difference caused online by the trigger, and $\eta_{\mathrm{NN}}=\eta(p_{\mathrm{e}}|\mathrm{NN})$ parametrizes any acceptance difference introduced by the NN (see Section 5.2). The $\mathrm{e}^+\pi^-\nu$ events were then distributed in three categories, depending on which offline decay tracks had been *seen* by the trigger, that is, were matched with a track in the trigger simulation. Different values of η (dependent on the momentum of the particles involved) corresponded to each category: when only the electron was seen (η_{e}, 14% of the events), or only the pion (η_π, 17% of the events), or both electron and pion ($\eta_{\mathrm{e}\pi}$, 69% of the events). In each class, decay particles entering the event selection through parameters not dependent on the track charge do not contribute to the corresponding η. The evaluation of these quantities was based on the following

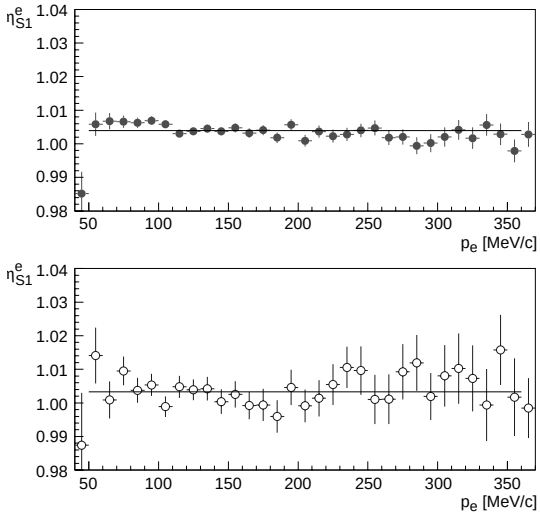

Figure 16: $\eta^{\rm e}_{\rm S1}$ for real (•) and simulated (○) data (see text) as a function of electron momentum $p_{\rm e}$.

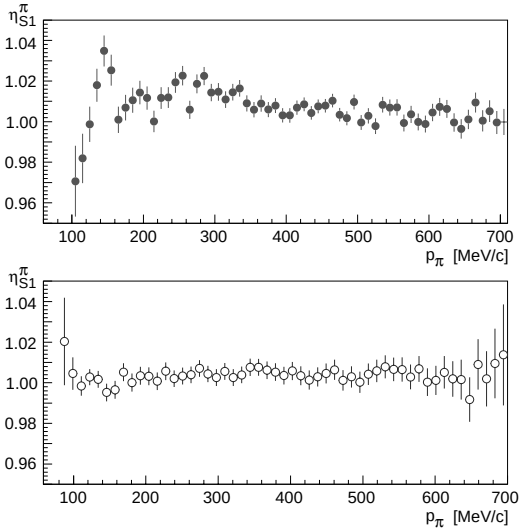

Figure 17: $\eta^{\pi}_{\rm S1}$ for real (•) and simulated (○) data (see text) as a function of pion momentum p_π.

relationships:

$$\begin{aligned}
\eta_{\rm e}(p_{\rm e},p_\pi) &= \frac{\epsilon({\rm e}^-|{\rm S1})}{\epsilon({\rm e}^+|{\rm S1})}\times\frac{\epsilon({\rm e}^-|{\rm OL})}{\epsilon({\rm e}^+|{\rm OL})}\times\frac{1-\epsilon(\pi^+|{\rm S1})\epsilon(\pi^+|{\rm OL})}{1-\epsilon(\pi^-|{\rm S1})\epsilon(\pi^-|{\rm OL})}\times\frac{\epsilon({\rm e}^-|{\rm NN})}{\epsilon({\rm e}^+|{\rm NN})}\,,\\
\eta_{\pi}(p_{\rm e},p_\pi) &= \frac{\epsilon(\pi^+|{\rm S1})}{\epsilon(\pi^-|{\rm S1})}\times\frac{\epsilon(\pi^+|{\rm OL})}{\epsilon(\pi^-|{\rm OL})}\times\frac{1-\epsilon({\rm e}^-|{\rm OL})}{1-\epsilon({\rm e}^+|{\rm OL})}\times\frac{\epsilon({\rm e}^-|{\rm S1})}{\epsilon({\rm e}^+|{\rm S1})}\times\frac{\epsilon({\rm e}^-|{\rm NN})}{\epsilon({\rm e}^+|{\rm NN})}\,,\\
\eta_{{\rm e}\pi}(p_{\rm e},p_\pi) &= \frac{\epsilon({\rm e}^-|{\rm S1})}{\epsilon({\rm e}^+|{\rm S1})}\times\frac{\epsilon({\rm e}^-|{\rm OL})}{\epsilon({\rm e}^+|{\rm OL})}\times\frac{\epsilon({\rm e}^-|{\rm NN})}{\epsilon({\rm e}^+|{\rm NN})}\times\frac{\epsilon(\pi^+|{\rm S1})}{\epsilon(\pi^-|{\rm S1})}\times\frac{\epsilon(\pi^+|{\rm OL})}{\epsilon(\pi^-|{\rm OL})}\,.
\end{aligned}$$

- $\eta_{\rm S1}$ – An S1 signal was needed for a track to be seen by the trigger and/or to enter NN. The electron and pion contributions to $\eta_{\rm S1}$ were studied separately. Thus, Fig. 16 shows $\eta^{\rm e}_{\rm S1}=\epsilon({\rm e}^-|{\rm S1})/\epsilon({\rm e}^+|{\rm S1})$ as a function of $p_{\rm e}$ for real and simulated data. The two distributions, fitted with a constant (1.0041 $\pm$ 0.0003 and 1.0034 $\pm$ 0.0008, respectively) are in good agreement. For pions, the dependence of $\eta^{\pi}_{\rm S1}=\epsilon(\pi^+|{\rm S1})/\epsilon(\pi^-|{\rm S1})$ on p_π is shown in Fig. 17. The weighted average between 100 and 450 MeV/c (where most of the decay pions lie) is 1.011 $\pm$ 0.001 for real data, and 1.0033 $\pm$ 0.0008 for simulated data. We note that the simulation included no parametrization of the strong interaction dependence on the charge of the interacting particles. This explains why $\eta^{\pi}_{\rm S1}$ shows a structure only in real data.

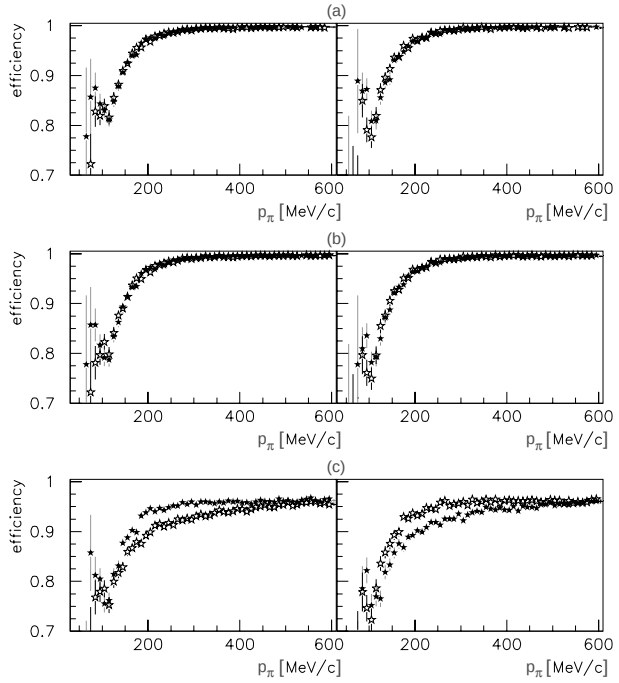

Figure 18: The trigger acceptance for real pions (see text), positive (black star) and negative (white star), in magnetic fields of opposite polarity, positive (left) and negative (right), as a function of pion momentum p_π at successive trigger stages: (a) coarse identification of track candidates, (b) fine-grain tracking, (c) track parametrization and selection of events with the correct number of primaries and secondaries.

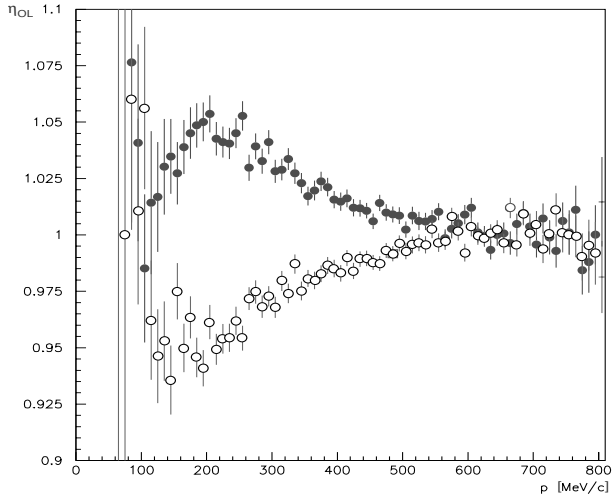

Figure 19: $\eta_{\rm OL} = \mathcal{P}_{t^+}/\mathcal{P}_{t^-}$ as measured for real pions (see text) in magnetic fields of opposite polarity, positive (●) and negative (○), as a function of track momentum p.

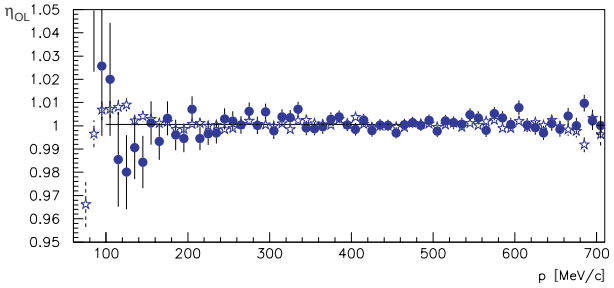

Figure 20: $\eta_{\rm OL} = \mathcal{P}_{t^+}/\mathcal{P}_{t^-}$ as measured from real (•) and simulated ($\star$) events (see text) summing data collected with the two magnetic-field polarities, as a function of track momentum p.

- $\eta_{\rm OL}$ – The contribution to η resulting from the trigger selection was investigated by letting pions from the minimum-bias T1 sample go through the trigger simulation. The Tγ sample was not used because, in this sample, the $\rm e^+e^-$ pair had been selected by asking for a very small opening angle ($\cos(\theta) > 0.995$), and tracks which are too close in space were not handled well by the trigger. Since kaons were very scarce in the T1 sample, the charged kaon, with a $p_{\rm T}$ value above threshold, requested at the very early stage, was mimicked by ignoring the Cherenkov signal of one of the four tracks. This track was chosen at random, with no consequent bias for later stages (the PID information was no longer needed). Owing to trigger characteristics [24], with electron and pion tracks being handled identically, the quantity of interest was the probability for a track with an S1 hit to be seen by the trigger, independently of whether the track was actually a pion or an electron. This probability was measured as a function of the track charge and momentum, $\mathcal{P}_{t^\pm}(p)$. For the sample considered, each track with an S1 hit was followed through the various trigger stages. Figure 18 shows the acceptance for successive trigger levels, each imposing a stricter track definition, as a function of the track charge and momentum, and magnetic field polarity. Tracks which were matched at every trigger stage formed the final sample and were used to calculate $\eta_{\rm OL} = \mathcal{P}_{t^+}/\mathcal{P}_{t^-}$ as a function of the track momentum, see Fig. 19. The shape of the momentum dependence reverses with the magnetic field polarity showing a preference for the positive-curvature tracks to be found by the trigger with respect to the negative-curvature tracks (see also Section 6.2). When we sum the data from the two magnetic-field polarities the geometrical effect cancels, see Fig. 20. In this case, in the momentum range from 100 to 450 $\rm MeV/\mathit{c}$, the real and simulated distributions of $\eta_{\rm OL}$ were fitted with constants of values 1.0006 ± 0.0006 and 1.0008 ± 0.0002, respectively. The track radial distributions of minimum-bias and $\rm e\pi\nu$ data differ, as all tracks of the former sample originated at the centre of the detector, while the neutral-kaon decay tracks could originate at any radius. However, when the procedure described above was applied to simulated $\rm e\pi\nu$ data, no radial dependence was found.
- $\eta_{\rm NN}$ – The analysis demanded one and only one track to be identified as an electron. Events where both secondary tracks were identified as electrons were rejected. To first order, $\eta_{\rm NN}$ coincides with the electron contribution $\eta^{\rm e}_{\rm NN}$ originating from electron identification. Using real pions of the minimum-bias sample, it was determined that the probability of a pion to be misidentified as an electron was (1.03 ± 0.01) times greater for positive than for negative pions. This small charge asymmetry had a negligible effect on the evaluation of η, but was taken into account in the background evaluation, see Section 6.5. Figure 21 shows $\eta_{\rm NN} = \eta^{\rm e}_{\rm NN}$ for real and simulated data as a function of electron momentum. Between 50 $\rm MeV/\mathit{c}$ and 250 $\rm MeV/\mathit{c}$, the real and simulated distributions were fitted with constants of value 1.0002 ± 0.0005 and 1.0017 ± 0.0011, respectively. The slight increase of $\eta^{\rm e}_{\rm NN}$ above 250 $\rm MeV/\mathit{c}$ was reproduced by a simulation including δ-rays production.

The weighted averages over the real events of each category were $\langle\eta_{\rm e}\rangle = 0.926 \pm 0.008$, $\langle\eta_\pi\rangle = 1.017 \pm 0.010$, and $\langle\eta_{\rm e\pi}\rangle = 1.015 \pm 0.021$. For the complete set of events, the weighted average was $\langle\eta\rangle = 1.014 \pm 0.002$. These values, however, did not enter the analysis since to each event was applied an individual weight, as determined from real calibration data. The whole procedure was verified by

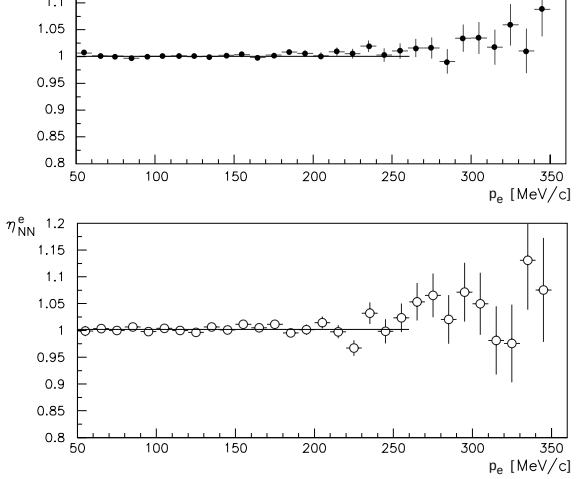

Figure 21: $\eta^{\rm e}_{\rm NN}$ for real (•) and simulated (○) data (see text) as a function of electron momentum $p_{\rm e}$. The continuous lines are the results of a fit with a constant.

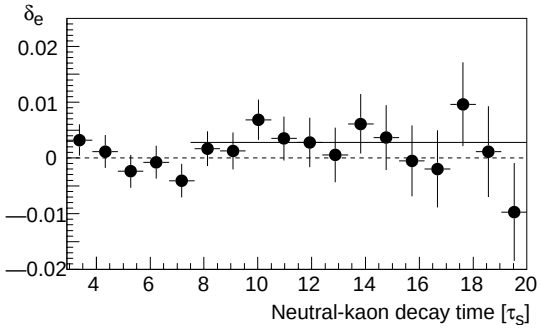

Figure 22: The charge asymmetry $\delta_{\rm e}$ (real data), see text. The continuous line is the result of a fit with a constant.

measuring the $\rm K_L$ charge asymmetry $\delta_{\rm e}$. This $\mathcal{CP}$-violating parameter [22] was obtained from the rate asymmetry $A_{\rm C}^{\rm exp}$ and its phenomenological expression $A_{\rm C}$ (in the limit of negligible background):

$$A_{\rm C}^{\rm exp}(\tau) = \frac{[\overline{N}_{w+}(\tau)+\alpha N_{w+}(\tau)]-[\overline{N}_{w-}(\tau)+\alpha N_{w-}(\tau)]}{[\overline{N}_{w+}(\tau)+\alpha N_{w+}(\tau)]+[\overline{N}_{w-}(\tau)+\alpha N_{w-}(\tau)]},$$
$$A_{\rm C}(\tau) = \frac{[\overline{R}_{+}(\tau)+\alpha R_{+}(\tau)]-[\overline{R}_{-}(\tau)+\alpha R_{-}(\tau)]}{[\overline{R}_{+}(\tau)+\alpha R_{+}(\tau)]+[\overline{R}_{-}(\tau)+\alpha R_{-}(\tau)]},$$

with $A_{\rm C}=\delta_{\rm e}$ in the limit of $\tau \gg \tau_{\rm S}$. The results are shown in Fig. 22. Fitting the data above 8 $\tau_{\rm S}$ with a constant, we obtained $\delta_{\rm e}=(3.8\pm1.2)\times10^{-3}$. Our measurement is in good agreement with the world average of Ref. [7], $\delta_{\rm e}=(3.33\pm0.14)\times10^{-3}$ although subject to a large statistical error (see footnote 2). $A_{\rm C}^{\rm exp}$ is directly proportional to η and a variation $\Delta(\eta)$ on η translates into a variation $\Delta(\delta_{\rm e})=1/2\Delta(\eta)$ on $\delta_{\rm e}$.

6.4 Correlations between track detection efficiencies – ω normalization

Special care was taken to minimize any detection efficiency correlation between tracks, and track isolation criteria were applied to avoid such correlations both at the online selection and in the offline analysis. Only in the case of the $A_{\Delta m}^{\rm exp}$ asymmetry, where 'opposite curvature' events are compared, see Section 7.4, a third normalization factor, ω, was needed. This parameter is the ratio of the efficiencies for detecting events with a primary charged kaon and a decay electron of equal and opposite curvature sign, $\omega \equiv \epsilon({\rm K^{\pm}e^{\mp}})/\epsilon({\rm K^{\pm}e^{\pm}})$, and accounts for curvature correlation effects. We have ensured with a high-statistics simulation that ω was equal to unity (with an error of $\pm4\times10^{-4}$) for the data sample taken with the trigger (less restrictive) including PC0 (Section 4.2), see Fig. 23a. For earlier data samples, obtained with a more restrictive trigger, a small bias ($\omega = 0.9957 \pm 0.0009$) was observed at early ($< 3.5\ \tau_{\rm S}$)

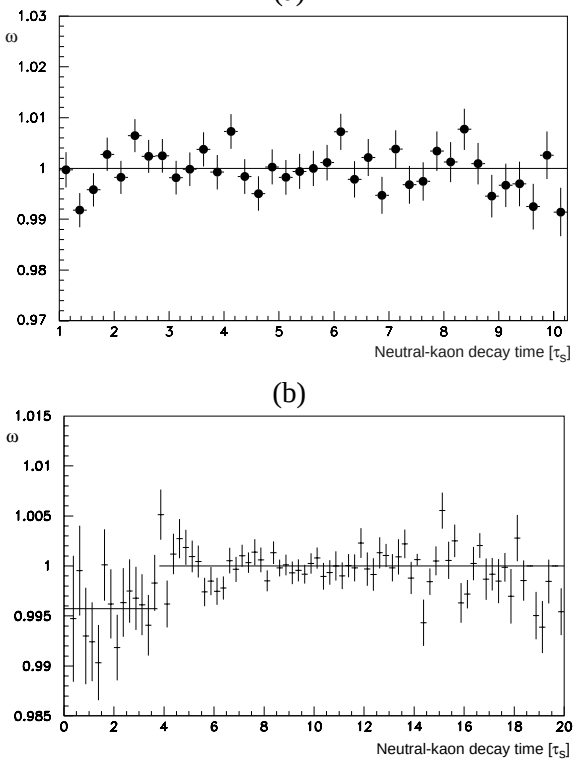

Figure 23: ω as a function of neutral-kaon decay time: simulated data (a) with relaxed trigger conditions (owing to PC0), after analysis cuts; (b) after simulating on these data the more restrictive trigger (no PC0). The continuous lines are fit results in the intervals (a) $(1-10)\ \tau_{\rm S}$, (b) $(0-3.5)\ \tau_{\rm S}$ and $(3.5-20)\ \tau_{\rm S}$.

decay times (see Fig. 23b), and corrected for. This bias was evaluated by simulating the restrictive trigger decision on the unbiased simulated sample.

6.5 Background determination

High-statistics simulated data were generated with the GEANT 3.15 package [31]. The golden $\overline{\rm p}{\rm p}$ annihilation channel was selected and particle momenta generated according to the available phase space and known production matrix elements. The intermediate resonances ${\rm K}^{\pm *}$ and ${\rm K}^{0*}$ were also simulated. Decay events were generated and weighted with known ${\rm K_S}$ and ${\rm K_L}$ branching ratios (BR) [7]: 68.6% of ${\rm K_S}$ decay to $\pi^+\pi^-$, 31.3% to $\pi^0\pi^0$, and 0.07% to ${\rm e}\pi\nu$; 38.8% of ${\rm K_L}$ decay to ${\rm e}\pi\nu$, 27.2% to $\mu\pi\nu$, and 21.1 % to $3\pi^0$, 12.6 % to $\pi^+\pi^-\pi^0$. Semileptonic (${\rm e}\pi\nu$ and $\mu\pi\nu$) event simulation included the V–A matrix elements and the linear-parameter form factor with $\lambda_+ = 0.03$ [7] . To obtain the background rates, the events from different decay channels were filtered through the complete analysis, including trigger simulation. The frequency distributions of the signal and background events (from different sources) are displayed in Fig. 24 as functions of the decay time, with no distinction between background associated with ${\rm K}^0$ and $\overline{\rm K}^0$, or opposite electron charge in the final state. The $\mu\pi\nu$ events, which were identified as ${\rm e}\pi\nu$ events, were considered as part of the signal. Hence, the latter is the sum of the number of events in Figs. 24a and 24b. The events where either the electron (or the muon) was misidentified as a pion, and vice versa, contribute to the background. In the following we list the various background components, and comment on them where appropriate.

– $\pi^+\pi^-$ decays (dominating at early decay times). Their amount was evaluated from the sample of simulated neutral-kaon decays to $\pi^+\pi^-$. The ${\rm e}\pi\nu$ selection criteria required that one pion was misidentified as an electron. The probability for that to happen was $\mathcal{P}(\pi|{\rm e}) = 2\%$ for pions of well measured momentum (Section 5.2). This could not be the case if the decay to $\pi^+\pi^-$ was fitted as a decay to ${\rm e}\pi\nu$. Figure 25 shows that for these events pions mimicking electrons have either decayed to muons or interacted in the PID material (for 2/3 of them). Since strong interactions are difficult to model, in order to account for a 'wrong' momentum, the PID response to pions in the simulation

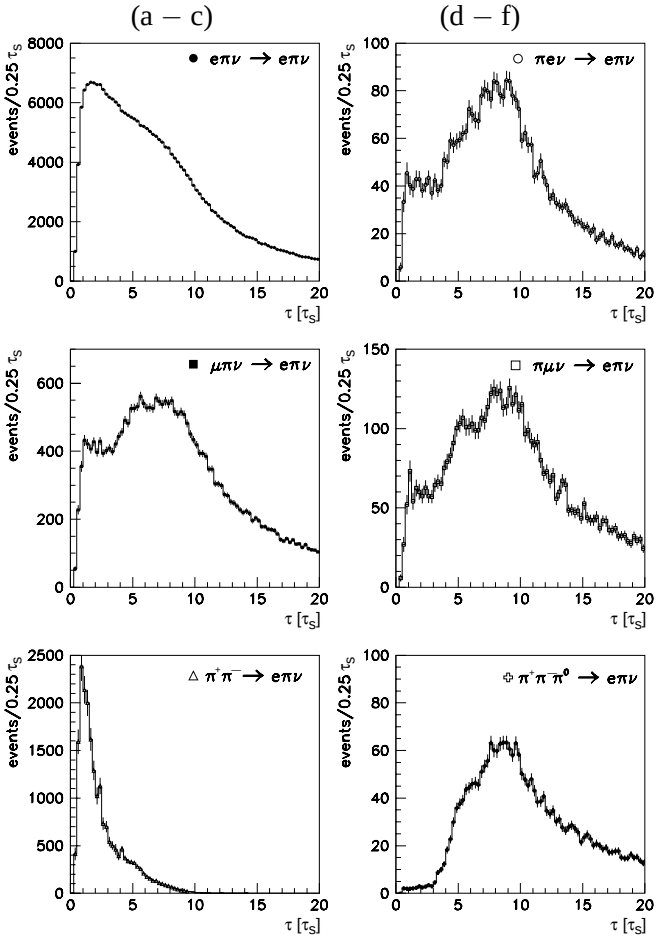

Figure 24: Distributions of the signal ($e\pi\nu$ and $\mu\pi\nu$) and background (see text) events, as determined from simulated data, as a function of neutral-kaon decay time τ. The $\pi^0\pi^0$ contribution (not shown) amounts to $\approx 1/2$ that of $\pi^+\pi^-$ with a similar time dependence.

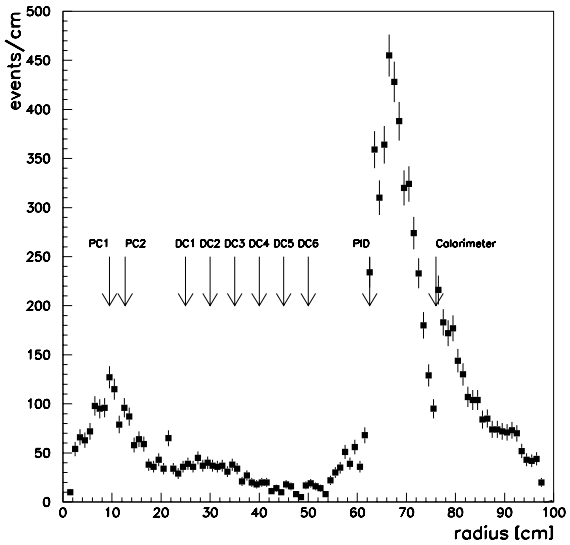

Figure 25: Radial distribution of a pion decay or interaction point for $\pi^+\pi^-$ events selected as $e\pi\nu$ (simulated data, see text).

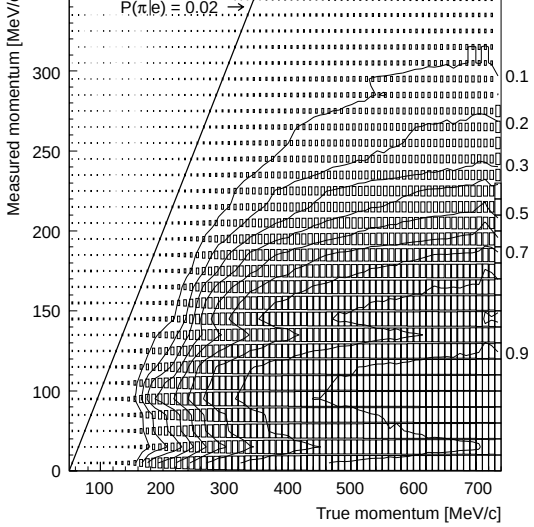

Figure 26: Probability $\mathcal{P}(\pi|\mathrm{e})$ that the neural network misidentifies a pion as an electron, as a function of particle's true and measured momentum: contour plot. Lines of equal probability (from 0.1 to 0.9) show that $\mathcal{P}(\pi|\mathrm{e})$ increases with the momentum error. The line $p_{\mathrm{meas}} = p_{\mathrm{true}}$ represents $\mathcal{P}(\pi|\mathrm{e}) = 0.02$.

was tuned using real $\pi^+\pi^-$ decays. The PID responses of pions with well-measured momenta from real $\pi^+\pi^-$ decays were input to the NN. For each pion, however, the momentum value given to the NN was shifted from the true value – assumed to be the value determined in the $\pi^+\pi^-$ analysis after the constrained fits – by an arbitrary amount. The probability of a pion being misidentified as an electron was determined as a function of this shift in momentum. The results of this are summarized in Fig. 26 where contours of misidentification probability are shown in a 2-D plot of true versus measured (i.e. shifted) momentum. In the simulated data, a pion's true momentum was taken as the generated value and its measured momentum as the value returned from the track fit. The probability of it being misidentified as an electron was then taken from the appropriate bin of true versus measured momentum, determined from real data as described above.

- $\pi^0\pi^0$ decays. As a result of a neutral-pion decay, an $\mathrm{e}^+\mathrm{e}^-$ pair may be produced, either directly (Dalitz decay) or by conversion of a decay photon. If in addition an electron is misidentified as a pion, such an event may contribute to the background.
- $\mathrm{e}\pi\nu$ and $\mu\pi\nu$ decays. These otherwise genuine events are classified as background if the decay particles are incorrectly assigned.
- $\pi^+\pi^-\pi^0$ decays. These are events where one of the charged pions fakes an electron, and the neutral pion accounts for the neutrino.

The $\mu\pi\nu$ contribution to the signal deserves some comments. According to the simulation, it amounts on average to 15% of the signal: It is 4% at the limits of the spectrum (40 and 350 MeV/c) and 20% in the 120–220 MeV/c range. The $\mu\pi\nu$ events are characterized by a decay-time resolution about 1.5 to 2 times worse than for genuine $\mathrm{e}\pi\nu$ events. This difference is included in the $\pm 10\%$ error attributed to the decay-time resolution and is accounted for in the systematic error. A worse decay-time resolution was expected since the $\mu\pi\nu$ events are reconstructed with a wrong lepton mass hypothesis (a similar effect is associated to the background events). Since the momenta of the particles emerging from the primary vertex are measured more accurately than the particles from the decay vertex, they constrain the event kinematics with a larger weight and the impact of the wrong event hypothesis is rather small.

Finally, the quantity entered in the fit procedure (Section 7.1) was the ratio between total background and signal, obtained as a function of the decay time as mentioned above. Background contributions relative to the signal are shown in Fig. 27a. Real and simulated data are compared in Fig. 27b, where the total background contribution is also displayed. The latter is on average 5% of the total (signal and background). The cuts on $\pi^+\pi^-$ decays to be described in Section 7.4 are also included in Fig. 27.

Tagging (or detection) efficiency differences at the primary vertex of background events were taken into account by the normalization factor ξ (Section 6.2). At the secondary vertex, the η normalization factor (Section 6.3) corrected for detection efficiency differences between final states containing

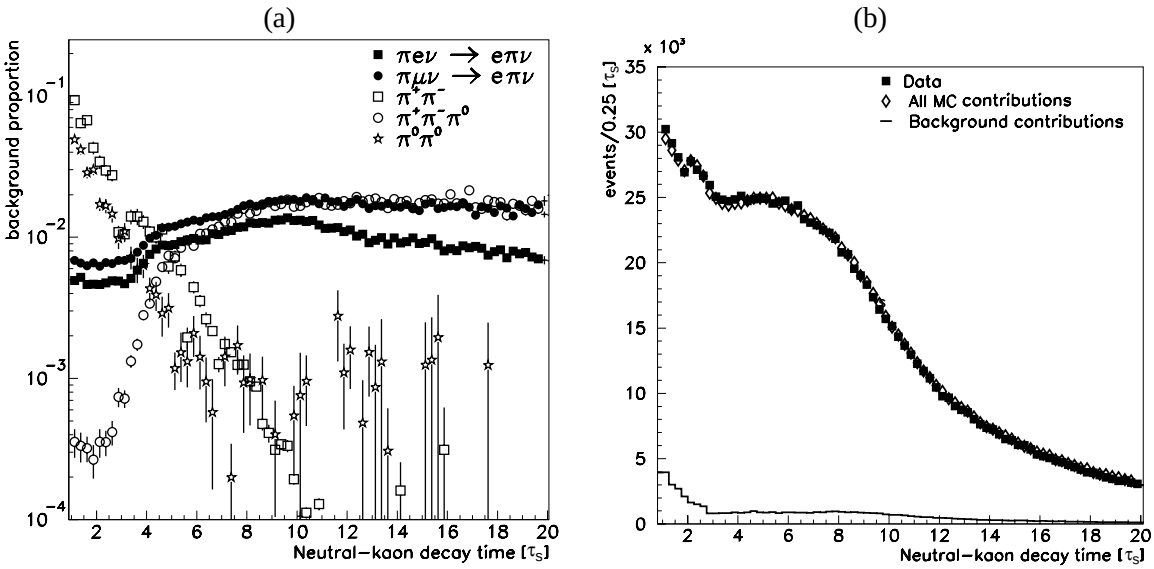

Figure 27: (a) Proportion of events from various background channels relative to the $e\pi\nu$ signal. (b) Decay-time distribution for real data (squares) and simulated data (open diamonds). The expected background contribution is shown by the solid line.

$e^+\pi^-$ and $e^-\pi^+$ pairs. (The weights entering the background rates are the ones obtained by calibration simulated data, in much the same way as in the real data case.)

The difference between the probabilities for positive pions to be misidentified as positrons and negative pions as electrons (see Section 6.3) was also considered. The ratio of this difference to the mean probability value was measured to be on average 0.03 ± 0.01. This value was assumed as the ratio of the difference of the corresponding backgrounds to their mean (background charge asymmetry).

7 Results

7.1 Fit procedure

The measured asymmetries of Eq. (17a – 17c) were fitted in the decay-time interval between 1 and 20 τ_S, with the corresponding phenomenological asymmetries of Eq. (18a –18c) folded with the time resolution and including the ratio between total background and signal, as given by the simulation. In all cases the parameters $\Gamma_S = \hbar/\tau_S$ and $\Gamma_L = \hbar/\tau_L$ were fixed to world-average values with $\tau_S = (0.8934 \pm 0.0008) \times 10^{-10}$ s, and $\tau_L = (5.17 \pm 0.04) \times 10^{-8}$ s [26]. The parameter Δm, when not considered a free parameter of the fit, was fixed to the world-average value $\Delta m = (530.1 \pm 1.4) \times 10^7 \hbar$ s^{-1} [26] which includes a subset of the CPLEAR measurements.

7.2 Consistency of results

The data presented in this paper were collected in separate data-taking periods between 1992 and 1995. Fits performed separately for each data-taking period allowed us to check the internal consistency of the data, as shown in Fig. 28.

7.3 Systematic errors

The following sources of systematic error have been investigated.

- Background level and charge asymmetry. As mentioned in Section 6.5, the relative acceptances for various background contributions were determined with a Monte Carlo simulation. By changing the analysis cuts on real and simulated data, the limits within which these acceptances are known were estimated to be $\pm 10\%$. Uncertainties on the branching ratios and form-factor are included in this error. The error of the background charge asymmetry (see Section 6.5) is dominated by statistics and estimated to be ± 0.01.
- Normalization corrections. The knowledge of the normalization corrections, ξ and η, is limited by the statistics available from calibration samples.

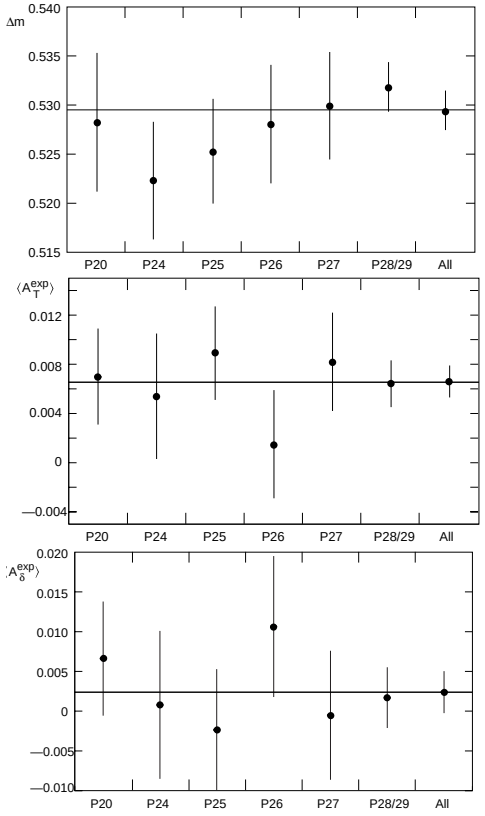

Figure 28: Δm, $\langle A_{\rm T}^{\rm exp}\rangle$ and $\langle A_{\delta}^{\rm exp}\rangle$ measured for different running periods (P20 and from P24 to P28/29) together with the final value.

- Regeneration correction. The evaluation of the systematic error resulting from the regeneration correction was performed by altering the Δf values along the one-standard-deviation ellipse in the complex plane $[{\rm Re}(\Delta f), {\rm Im}(\Delta f)]$, as determined by CPLEAR [30].
- Decay-time resolution. The decay-time resolution was determined from a Monte Carlo simulation. Its accuracy was estimated to be better than 10%, and affects only the measurement of ${\rm Re}(x_+)$ extracted from the $A_{\Delta m}$ asymmetry. The systematic error resulting from the decay-time resolution was estimated by folding the resolution distribution to the asymmetry under study.
- Absolute time-scale. Extensive studies have shown that after the kinematic constrained fits, the absolute time-scale is known with a precision of $\Delta\tau/\tau = \pm 2 \times 10^{-4}$ [32].

The effects of the above contributions are summarized in Tables 3, 5, 6 for the $A_{\Delta m}$, $A_{\rm T}$ and A_{δ} analyses, respectively, together with the systematic errors arising from the phenomenological parameters used in the fit. The systematic errors were evaluated by allowing the value of each error source to vary within its uncertainty during the fit procedure.

7.4 $A_{\Delta m}$ asymmetry analysis

The parameters of interest become apparent when we write Eq. (18c) in the limit of negligible background:

$$A_{\Delta m}(\tau) \;=\; \frac{\cos(\Delta m\tau) - 2{\rm Im}(x_-)\sin(\Delta m\tau)}{\cosh(\Delta\Gamma\tau/2) - 2{\rm Re}(x_+)\sinh(\Delta\Gamma\tau/2)}\,. \tag{22}$$

For this specific analysis, which requires the lowest possible background at early decay time, additional cuts were applied. A minimum angle of 30° was required between any two tracks because of a pattern recognition inefficiency observed if the tracks were too close. The four-momentum squared, q^2, transferred from kaon to pion must be greater than the pion squared mass (the q^2 value corresponding to the $\pi^+\pi^-$ final state). Figure 29 shows the q^2 distribution for $\pi^+\pi^-$ events, analysed as $e\pi\nu$ events (contributing to background), and for semileptonic events (contributing to signal); the first distribution

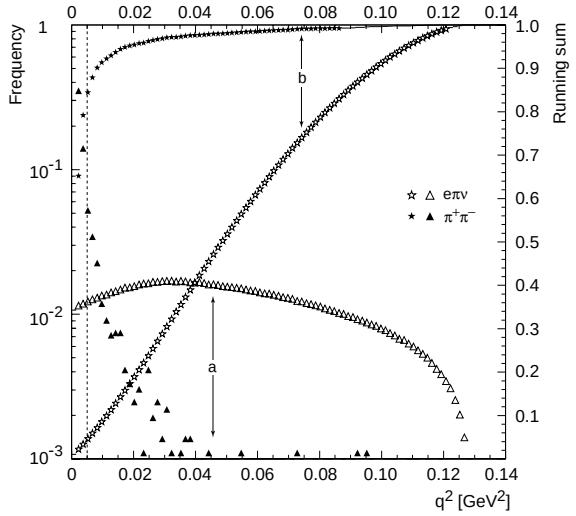

Figure 29: Simulated $\mathrm{e}\pi\nu$ and $\pi^+\pi^-$ events fitted with the $\mathrm{e}\pi\nu$ hypothesis: q^2, the four-momentum squared transferred from neutral kaon to pion. Distributions of (a) relative-frequency density and (b) relative-frequency running sum. The dotted line indicates the cut position.

Table 3: Summary of systematic errors on the results from the $A_{\Delta m}^{\mathrm{exp}}$ asymmetry. An asterisk denotes that a relative precision is given.

Source	Precision	Δm $[10^{10}\hbar/\mathrm{s}]$	$\mathrm{Re}(x_+)$ $[10^{-3}]$
Background level *	$\pm 10\%$	± 0.0002	± 4.4
Background asymmetry	± 0.01		
Normalization ($\alpha\xi$)	$\pm 3.4 \times 10^{-4}$		
and		± 0.0001	± 0.1
Normalization (η)	$\pm 2.0 \times 10^{-3}$		
Normalization (ω)	$\pm(4-9) \times 10^{-4}$	± 0.0001	—
Decay-time resolution *	$\pm 10\%$	± 0.0001	± 0.3
Absolute time-scale *	$\pm 2 \times 10^{-4}$	± 0.0001	± 0.3
Regeneration	Ref. [30]	—	—
$\tau_{\mathrm{S}} = 1/\Gamma_{\mathrm{S}}$	$\pm 0.08 \times 10^{-12}$ s	± 0.0001	± 0.7
Total syst.		± 0.0003	± 4.5

peaks around zero since one of the pions is wrongly attributed the electron mass. Cutting at 0.005 GeV^2 decreases the amount of $\pi^+\pi^-$ background by a factor four while only 5% of $\mathrm{e}\pi\nu$ events are lost. After including the background rates, Eq. (18c) folded with the decay-time resolution was fitted to the data $A_{\Delta m}^{\mathrm{exp}}(\tau)$, with Δm and $\mathrm{Re}(x_+)$ as free parameters, and $\mathrm{Im}(x_-) = 0$ (that is $\mathcal{CPT}$ invariance was assumed for possible $\Delta S \neq \Delta Q$ decay amplitudes). The systematic errors on Δm and $\mathrm{Re}(x_+)$ are summarized in Table 3. We note the following.

- Since in the construction of $A_{\Delta m}$ all terms linear in the regeneration corrections cancel, there is no systematic error from that source.
- Again by the asymmetry construction, systematic errors arising from normalization factors may be neglected.
- Since Δm is proportional to the frequency of the $\mathrm{K}^0 \rightleftharpoons \overline{\mathrm{K}}^0$ oscillation, this measurement is very sensitive to the absolute time-scale precision.
- Folding the decay-time resolution distribution to the $A_{\Delta m}$ asymmetry results in a shift of $+0.0013\times 10^{10}\,\hbar/\mathrm{s}$ for the value of Δm and -2.9×10^{-3} for the value of $\mathrm{Re}(x_+)$. The uncertainty on this correction was estimated to be $\pm 10\%$.
- The $A_{\Delta m}$ asymmetry is sensitive to a possible correlation in the detection efficiencies of the primary charged kaon and the decay electron, see Section 6.4. This required a normalization factor ω for a part of the data with an overall correction for Δm of $+0.0006 \pm 0.0001 \times 10^{10}\,\hbar/\mathrm{s}$.

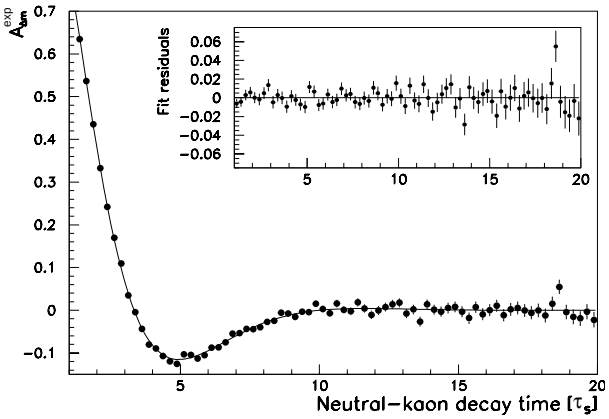

Figure 30: The $A_{\Delta m}^{\rm exp}$ asymmetry versus the neutral-kaon decay time (in units of $\tau_{\rm S}$). The solid line represents the result of the fit. Fit residuals are shown in the inset.

The measured asymmetry, together with the fitted function, is displayed in Fig. 30. Fit residuals are shown in the inset. The starting point of the fit was determined according to the sensitivity of the asymmetry to the residual background. Our final results are the following:

$$\begin{aligned}
\Delta m &= (0.5295 \pm 0.0020_{\rm stat} \pm 0.0003_{\rm syst}) \times 10^{10}\,\hbar/{\rm s}, \\
{\rm Re}(x_+) &= (-1.8 \pm 4.1_{\rm stat} \pm 4.5_{\rm syst}) \times 10^{-3}, \\
\chi^2/{\rm ndf} &= 0.94\,, \quad {\rm ndf} = 606\,.
\end{aligned}$$

The correlation coefficient between Δm and ${\rm Re}(x_+)$ is equal to 0.40. This Δm measurement is the most accurate single value contributing to the present world average [7]. The ${\rm Re}(x_+)$ measurement improves the current limit on a possible violation of the $\Delta Q = \Delta S$ rule by a factor three.

It is not possible to disentangle the two oscillating terms, which produce a correlation > 0.99 between Δm and ${\rm Im}(x_-)$. Assuming $\Delta m = (530.1 \pm 1.4) \times 10^7\,\hbar/{\rm s}$ (the world average), we obtain ${\rm Im}(x_-) = (-0.8 \pm 3.5) \times 10^{-3}$.

7.5 A_δ asymmetry analysis

In this case, the fitting equation, Eq. (18b), becomes, in the limit of negligible background,

$$\begin{aligned}
A_\delta(\tau) &= 4{\rm Re}(\delta) + 4\frac{{\rm Re}(\delta)\sinh(\Delta\Gamma\tau/2) + {\rm Im}(\delta)\sin(\Delta m\tau)}{\cosh(\Delta\Gamma\tau/2) + \cos(\Delta m\tau)} \\
&\quad -4\frac{{\rm Re}(x_-)\cos(\Delta m\tau)\sinh(\Delta\Gamma\tau/2) - {\rm Im}(x_+)\sin(\Delta m\tau)\cosh(\Delta\Gamma\tau/2)}{[\cosh(\Delta\Gamma\tau/2)]^2 - [\cos(\Delta m\tau)]^2}\,. \qquad (23)
\end{aligned}$$

After including the background, Eq. (18b) folded with the decay-time resolution was fitted to the data $A_\delta^{\rm exp}(\tau)$, with ${\rm Re}(\delta)$, ${\rm Im}(\delta)$, ${\rm Re}(x_-)$ and ${\rm Im}(x_+)$ as free parameters. The measured asymmetry $A_\delta^{\rm exp}$, together with the fitted function, is displayed in Fig. 31. Our final results are the following:

$$\begin{aligned}
{\rm Re}(\delta) &= (\ \ 3.0 \pm 3.3_{\rm stat} \pm 0.6_{\rm syst}) \times 10^{-4}\,, \\
{\rm Im}(\delta) &= (-1.5 \pm 2.3_{\rm stat} \pm 0.3_{\rm syst}) \times 10^{-2}\,, \\
{\rm Re}(x_-) &= (\ \ 0.2 \pm 1.3_{\rm stat} \pm 0.3_{\rm syst}) \times 10^{-2}\,, \\
{\rm Im}(x_+) &= (\ \ 1.2 \pm 2.2_{\rm stat} \pm 0.3_{\rm syst}) \times 10^{-2}\,, \\
\chi^2/{\rm ndf} &= 1.14\,, \quad {\rm ndf} = 604\,.
\end{aligned}$$

The correlation coefficients of the fit are shown in Table 4. We note that ${\rm Re}(x_-)$ and ${\rm Im}(x_+)$ are compatible with zero, which is expected in the case where the $\Delta S = \Delta Q$ rule holds. When we fix ${\rm Re}(x_-) = {\rm Im}(x_+) = 0$ in the fit, we obtain

$$\begin{aligned}
{\rm Re}(\delta) &= (\ \ 2.9 \pm 2.6_{\rm stat} \pm 0.6_{\rm syst}) \times 10^{-4}\,, \\
{\rm Im}(\delta) &= (-0.9 \pm 2.9_{\rm stat} \pm 1.0_{\rm syst}) \times 10^{-3}\,,
\end{aligned}$$

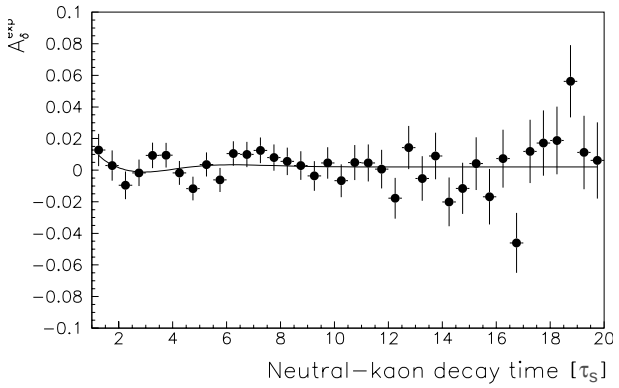

Figure 31: The $A_\delta^{\rm exp}$ asymmetry versus the neutral-kaon decay time (in units of $\tau_{\rm S}$). The solid line represents the result of the fit.

Table 4: The correlation coefficients from the A_δ fit.

	$\mathrm{Re}(\delta)$	$\mathrm{Im}(\delta)$	$\mathrm{Re}(x_-)$	$\mathrm{Im}(x_+)$
$\mathrm{Re}(\delta)$	–	0.44	-0.56	-0.60
$\mathrm{Im}(\delta)$		–	-0.97	-0.91
$\mathrm{Re}(x_-)$			–	0.96
$\mathrm{Im}(x_+)$				–

that is a negligible change for $\mathrm{Re}(\delta)$, but an error of $\mathrm{Im}(\delta)$ smaller by an order of magnitude. The correlation coefficient is -0.5. We stress that the analysis of the $\pi^+\pi^-$ decay channel [29] gives exactly the quantity $\alpha\xi = (1+4\mathrm{Re}(\varepsilon-\delta))\xi$ which enters the asymmetry presented here, and no external experimental information is needed for the quantity $\mathrm{Re}(\varepsilon-\delta)$. On average we have $\langle\alpha\xi\rangle = 1.12756\pm0.00034$. The A_δ asymmetry depends only weakly on η. The level of the background contributions remains below 1% of the signal. The regeneration corrections result in a shift of the $A_\delta^{\rm exp}$ value of the order of 0.3×10^{-3}. The systematic errors are shown in detail in Table 5. The dependence of the fit results on Δm, $\Gamma_{\rm S}$ and $\Gamma_{\rm L}$ is negligible within their respective errors. From Table 5 we conclude that the main systematic error on $\mathrm{Re}(\delta)$ results from the uncertainty in the normalization factor $\alpha\xi$, while $\mathrm{Im}(\delta)$, $\mathrm{Re}(x_-)$ and $\mathrm{Im}(x_+)$ are mainly affected by the uncertainty in the background charge asymmetry. In the case of the fit with two parameters, the systematic error on $\mathrm{Re}(\delta)$ is the same while the systematic error on $\mathrm{Im}(\delta)$ becomes three times smaller.

Table 5: Summary of systematic errors on the results from the $A_\delta^{\rm exp}$ asymmetry. An asterisk denotes that a relative precision is given.

Source	Precision	$\mathrm{Re}(\delta)$ $[10^{-4}]$	$\mathrm{Im}(\delta)$ $[10^{-2}]$	$\mathrm{Re}(x_-)$ $[10^{-2}]$	$\mathrm{Im}(x_+)$ $[10^{-2}]$
Background level *	$\pm10\%$	±0.1	±0.1	±0.1	±0.1
Background asymmetry	±0.01	±0.2	±0.3	±0.2	±0.3
Normalization $(\alpha\xi)$	$\pm3.4\times10^{-4}$	±0.5	±0.03	±0.02	±0.03
Normalization(η)	$\pm2.0\times10^{-3}$	±0.02	±0.03	±0.02	±0.03
Decay-time resolution *	$\pm10\%$	negligible	±0.1	±0.1	±0.1
Regeneration	Ref. [30]	±0.25	±0.02	±0.02	±0.02
Total syst.		±0.6	±0.3	±0.3	±0.3

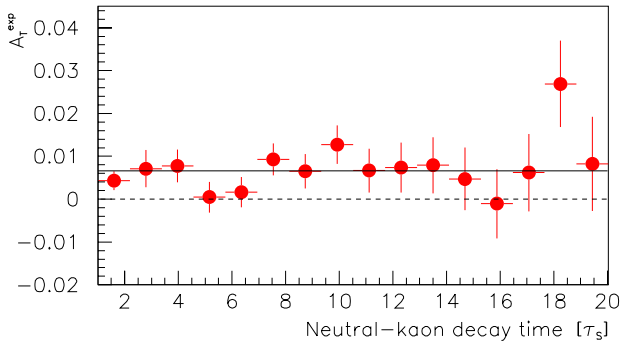

Figure 32: The asymmetry $A_{\rm T}^{\rm exp}$ versus the neutral-kaon decay time (in units of $\tau_{\rm S}$). The solid line represents the fitted average $\langle A_{\rm T}^{\rm exp}\rangle$.

Table 6: Summary of systematic errors on the results from the $A_{\rm T}^{\rm exp}$ asymmetry. An asterisk denotes that a relative precision is given.

Source	Precision	$\langle A_{\rm T}^{\rm exp}\rangle$ $[10^{-3}]$	$\mathrm{Im}(x_+)$ $[10^{-3}]$
Background level *	$\pm 10\%$	± 0.03	± 0.2
Background asymmetry	± 0.01	± 0.02	± 0.5
Normalization (ξ)	$\pm 4.3\times 10^{-4}$	± 0.2	± 0.1
Normalization (η)	$\pm 2.0\times 10^{-3}$	± 1.0	± 0.4
Decay-time resolution *	$\pm 10\%$	negligible	± 0.6
Regeneration	Ref. [30]	± 0.1	± 0.1
Total syst.		± 1.0	± 0.9

7.6 $A_{\rm T}$ asymmetry analysis

The $A_{\rm T}$ asymmetry represents a direct comparison of $\mathcal{T}$-conjugated rates. The measured asymmetry $A_{\rm T}^{\rm exp}$ is shown in Fig. 32. Between 1 and 20 $\tau_{\rm S}$ the data points scatter around a constant offset from zero, the average being

$$\begin{aligned}\langle A_{\rm T}^{\rm exp}\rangle &= (6.6\pm 1.3)\times 10^{-3}\,,\\ \chi^2/{\rm ndf} &= 0.84\,,\quad {\rm ndf}=607\,.\end{aligned}$$

This is an evidence for $\mathcal{T}$ violation. For a thorough analysis the appropriate phenomenological expression was used. In the limit of negligible background, the fitting equation, Eq. (18a), becomes

$$\begin{aligned}A_{\rm T}(\tau) &= 4(\mathrm{Re}(\varepsilon)-\mathrm{Re}(y)-\mathrm{Re}(x_-))\\ &+ 2\frac{\mathrm{Re}(x_-)(e^{-\frac{1}{2}\Delta\Gamma\tau}-\cos(\Delta m\tau))+\mathrm{Im}(x_+)\sin(\Delta m\tau)}{\cosh(\frac{1}{2}\Delta\Gamma\tau)-\cos(\Delta m\tau)}\,.\end{aligned}\qquad (24)$$

With respect to Eq. (14), we note on the r.h.s. an additional term $-2(\mathrm{Re}(x_-)+\mathrm{Re}(y))$. This term follows from the primary-vertex normalization procedure, see Section 6.2. Equation (24) simplifies when $\mathcal{CPT}$ invariance in the $e\pi\nu$ decay amplitudes is assumed ($\mathrm{Re}(y)=0$ and $\mathrm{Re}(x_-)=0$). We allowed, however, for a possible violation of the $\Delta S=\Delta Q$ rule ($\mathrm{Im}(x_+)\neq 0$). The fitting procedure then contains only two parameters, $\mathrm{Re}(\varepsilon)$ and $\mathrm{Im}(x_+)$, both $\mathcal{T}$ violating. After including the background rates, Eq. (18a) folded with the decay-time resolution was fitted to the data $A_{\rm T}^{\rm exp}(\tau)$. The final results are the following.

$$\begin{aligned}4\mathrm{Re}(\varepsilon) &= (6.2\pm 1.4_{\rm stat}\pm 1.0_{\rm syst})\times 10^{-3}\,,\\ \mathrm{Im}(x_+) &= (1.2\pm 1.9_{\rm stat}\pm 0.9_{\rm syst})\times 10^{-3}\,,\\ \chi^2/{\rm ndf} &= 0.84\,,\quad {\rm ndf}=606\,.\end{aligned}$$

The correlation coefficient between $4\mathrm{Re}(\varepsilon)$ and $\mathrm{Im}(x_+)$ is 0.46.

Thus $\mathcal{T}$ violation in the neutral-kaon mixing is clearly demonstrated. Since $\mathrm{Im}(x_+)$ is compatible with zero, no $\mathcal{T}$ violation is observed in the semileptonic decay amplitude which violates the $\Delta S=\Delta Q$

rule, should this amplitude be different from zero. We note that $\mathrm{Im}(x_+)$ is given by the values of the asymmetry at early decay times while $4\mathrm{Re}(\varepsilon)$ is determined by the late decay-time values. As a result the average $\langle A_{\mathrm{T}}^{\mathrm{exp}} \rangle$ between 1 and 20 τ_{S} is essentially equal to $4\mathrm{Re}(\varepsilon)$.

A summary of the systematic errors for the different parameters is reported in Table 6. Note that the systematic errors on $\langle A_{\mathrm{T}}^{\mathrm{exp}} \rangle$ also apply to $4\mathrm{Re}(\varepsilon)$ for the case of the two-parameter fit. The secondary-vertex normalization η is the dominant source of systematic error for this asymmetry. The decay-time resolution introduces a negligible change in $\langle A_{\mathrm{T}}^{\mathrm{exp}} \rangle$. The uncertainties on Δm, Γ_{S} and Γ_{L} are negligible in the fit.

8 Summary and conclusions

In order to study discrete symmetries the CPLEAR experiment performed a simultaneous comparison between strange-particle and strange-antiparticle properties. This was directly done measuring K^0 and $\overline{\mathrm{K}}^0$ decay rates (but also rates of interaction with matter), rather than $\mathrm{K_S}$ and/or $\mathrm{K_L}$ decay rates. The principle of some of the measurements then becomes straightforward, for instance the establishement of $\mathcal{T}$ non-invariance. In this paper we have described the application of the method in relation to the $\mathrm{e}\pi\nu$ decay channel in order to measure $\mathcal{T}$ and $\mathcal{CPT}$ parameters in the neutral-kaon system.

In summary, two strangeness states of the neutral kaons were tagged at production taking advantage of associate kaon-pair production in $\overline{\mathrm{p}}\mathrm{p}$ annihilation, and two charge configurations ($\mathrm{e}^+\pi^-$) and ($\mathrm{e}^-\pi^+$) characterized the final state of neutral-kaon decays. Four rates of semileptonic ($\mathrm{e}\pi\nu$) decays from K^0 and $\overline{\mathrm{K}}^0$ were measured as a function of the decay time. In order to minimize systematic errors three asymmetries were formed with these decay rates: A_{T}, A_δ and $A_{\Delta m}$. Two of the asymmetries, A_{T} and A_δ, flatten out at early decay times to a continuous level below 1%. The asymmetry $A_{\Delta m}$ instead shows a pronounced oscillatory behaviour.

The data analysis was performed along the same lines as the $\pi^+\pi^-$ analysis reported previously [29]. However, the following points deserved special care :

- The kinematics (three-body final states including a ν) was less constraining. As a result, to select the signal events and achieve background suppression, the identification of the final-state electron was necessary.
- The need for e/π separation introduces a potential bias between $\mathrm{e}^+\pi^-$ and $\mathrm{e}^-\pi^+$ final states. The efficiency ratio of these final states demanded precise calibrations.
- The $\mathrm{K}^0/\overline{\mathrm{K}}^0$ initial ratio was determined using the $\pi^+\pi^-$ events collected at early decay time in the same data-taking periods. Thus, systematic errors were minimized, but at the price of introducing in the analysis the parameter $\mathrm{Re}(\varepsilon - \delta)$. This quantity cancels by construction in the A_δ asymmetry (it also cancelled in the $\pi^+\pi^-$ asymmetry), and has no impact in the measurement of Δm. However, this is not the case for the asymmetry A_{T}. Here a careful discussion of the physics consequences is needed.
- The asymmetry behaviours for A_{T} and A_δ are not strongly time dependent, which renders the measurement more susceptible to normalization and efficiency effects, and less sensitive to the values of parameters such as Δm, Γ_{S} and Γ_{L}. The asymmetry $A_{\Delta m}$ however shows a large dependence on time (as was the case for the asymmetry measured in the $\pi^+\pi^-$ decay channel), thus allowing the measurement of Δm. The Δm measurement is in turn sensitive to Γ_{S} and to the absolute decay-time scale.
- The $\mathrm{e}\pi\nu$ statistics was lower by a factor 50 compared to the $\pi^+\pi^-$ sample: most of the reduction occurred because the $\mathrm{e}\pi\nu$ sample originates essentially from $\mathrm{K_L}$, of which only 3% decay within the fiducial volume of the CPLEAR detector.

Fitting the phenomenological expressions of these asymmetries to the data allowed a variety of parameters to be determined. In particular:

- A_{T} – The asymmetry A_{T} was measured for the first time and is well compatible with $4\mathrm{Re}(\varepsilon)$. In the limit of $\mathcal{CPT}$ invariance in the semileptonic decay process, this measurement demonstrates a violation of time-reversal invariance in the evolution of neutral kaons into their antiparticles, independently of the validity of the $\Delta S = \Delta Q$ rule. Effectively it manifests the difference of

$\mathcal{T}$-conjugated processes as the difference between the rate of oscillation from K^0 to $\overline{\mathrm{K}}^0$ and from $\overline{\mathrm{K}}^0$ to K^0. For a detailed discussion of the theoretical implications see Ref. [33].

- A_δ – We have directly measured $\mathcal{CPT}$ invariance through the parameters $\mathrm{Re}(\delta)$ and $\mathrm{Im}(\delta)$. Again we underline the direct approach (in contrast to an evaluation of $\mathrm{Im}(\delta)$ from various measurements, using the unitarity relation and resulting in an error smaller by two orders of magnitude [15]). It was the measurement of $\mathrm{Re}(\delta)$ which enabled us for the first time to set a limit to the K^0–$\overline{\mathrm{K}}^0$ decay-width difference, and to disentangle possible cancellation effects [16].
- $A_{\Delta m}$ – From the asymmetry $A_{\Delta m}$ we obtained the best individual measurement for Δm, which is one of the fundamental parameters of the neutral-kaon system.

Finally, the systematic errors affecting our measurements were shown to be smaller than the statistical ones.

Acknowledgements

We would like to thank the CERN LEAR staff for their support and co-operation, as well as the technical and engineering staff of our institutes. This work was supported by the following agencies: the French CNRS/Institut National de Physique Nucléaire et de Physique des Particules, the French Commissariat à l'Energie Atomique, the Greek General Secretariat of Research and Technology, the Netherlands Foundation for Fundamental Research on Matter (FOM), the Portuguese National Board for Science and Technology (JNICT), the Ministry of Science and Technology of the Republic of Slovenia, the Swedish Natural Science Research Council, the Swiss National Science Foundation, the UK Particle Physics and Astronomy Research Council (PPARC), and the US National Science Foundation.

References

[1] E. Gabathuler and P. Pavlopoulos, Proc. of the Workshop on Physics at LEAR with Low Energy Cooled Antiprotons (Erice, 1982), eds. U. Gastaldi and R. Klapisch (Plenum, New York, 1984) p. 747.

[2] A. Angelopoulos et al., CPLEAR Collaboration, Phys. Lett. B444 (1998) 38.

[3] A. Angelopoulos et al., CPLEAR Collaboration, Phys. Lett. B444 (1998) 43.

[4] A. Angelopoulos et al., CPLEAR Collaboration, Phys. Lett. B444 (1998) 52.

[5] V. Demidov et al., Phys. Atom. Nucl. 58 (1995) 568.

[6] R. Adler et al., CPLEAR Collaboration, Phys. Lett. B369 (1996) 367.

[7] D.E. Groom et al., Particle Data Group, Eur. Phys. J. C15 (2000) 1. (Data used before 2000 are thus cited if they remain unchanged.)

[8] M. Cullen et al., Phys. Lett. B32 (1970) 523.

[9] C. Geweniger et al., Phys. Lett. B52 (1974) 108.

[10] S. Gjesdal et al., Phys. Lett. B52 (1974) 113.

[11] L.K. Gibbons et al., E731, Phys. Rev. Lett. 70 (1993) 1198.

[12] B. Schwingenheuer et al., E773, Phys. Rev. Lett. 74 (1995) 4376.

[13] R. Adler et al., CPLEAR Collaboration, Phys. Lett. B363 (1995) 243 (these data are a subset of the total collected by CPLEAR).

[14] R. Adler et al., CPLEAR Collaboration, Phys. Lett. B363 (1995) 237 (these data are a subset of the total given in the present paper).

[15] A. Apostolakis et al., CPLEAR Collaboration, Phys. Lett. B456 (1999) 297.

[16] A. Angelopoulos et al., CPLEAR Collaboration, Phys. Lett. B471 (1999) 332.

[17] R. Adler et al., CPLEAR Collaboration, and J. Ellis, J.L. Lopez, N.E. Mavromatos, D.V. Nanopoulos, Phys. Lett. B364 (1995) 239.

[18] F. Benatti, R. Floreanini, Phys. Lett. B401 (1997) 337.

[19] H.-J. Gerber, Phys. Rev. Lett. 80 (1998) 2969.

[20] C. Geweniger et al., Phys. Lett. B48 (1974) 487.

[21] C.D. Buchanan et al., Phys. Rev. D45 (1992) 4088.

[22] L. Maiani, CP and CPT violation in neutral kaon decays, in The Second DAΦNE Physics Handbook, eds. L. Maiani et al. (INFN, Frascati, 1995) p. 3. (The parametrizations presented there are equivalent to ours but formulated in a slightly different notation.)

[23] A. Apostolakis et al., CPLEAR Collaboration, Phys. Lett. B473 (2000) 186.

[24] R. Adler et al., CPLEAR Collaboration, Nucl. Instrum. Methods A379 (1996) 76.

[25] L.-M. Chounet, J.-M. Gaillard and M.K. Gaillard, Phys. Rep. 4 (1972) 199.

[26] C. Caso et al., Particle Data Group, Eur. Phys. J. C3 (1998) 1.

[27] R. Adler et al., CPLEAR Collaboration, Nucl. Instrum. Methods A390 (1997) 293.

[28] Electron-muon-pion separation in the CPLEAR experiment using the Particle Identification Detector, Internal Note, CPLEAR/DET/95-02, Jan. 1995.

[29] A. Apostolakis et al., CPLEAR Collaboration, Eur. Phys. J. C18 (2000) 41.

[30] A. Angelopoulos et al., CPLEAR Collaboration, Phys. Lett. B413 (1997) 422.

[31] R. Brun et al., GEANT user's guide, CERN DD/EE/84-1, 1984.

[32] Determination of the position accuracy in CPLEAR, Internal Note, CPLEAR/DET/96-03, October 1996.

[33] L. Alvarez-Gaumé et al., Phys. Lett. B458 (1999) 347, and references quoted therein.